Elsevier Editorial System(tm) for Ceramics International

Manuscript Draft

Manuscript Number: CERI-D-18-09111R3

Title: Nanostructural changes upon substitutional Al doping in ZnO sputtered films

Article Type: Full length article

Keywords: TCO; ZnO; Al doping; nanostructure

Corresponding Author: Dr. Mercedes Gabas, Dr.

Corresponding Author's Institution: University of Málaga

First Author: Angel R Landa-Cánovas, Dr.

Order of Authors: Angel R Landa-Cánovas, Dr.; José Santiso, Prof.; Fernando Agulló-Rueda, Dr.; Pilar Herrero, Dr.; Elena Navarrete-Astorga, Dr.; Efraín Ochoa-Martínez, Dr.; José R Ramos-Barrado, Prof.; Mercedes Gabas, Dr.

Abstract: Al:ZnO layers, with low and high Al content, -0.2% cat. and 2.1% cat. respectively-, have been prepared using the RF magnetron sputtering technique. Noticeable differences in the optical and electrical properties have been detected in these films. With doping, the resistivity decreases and the band-gap increases. The alterations in the films crystalline structure are explained in terms of the nanostructural changes induced by Al substitutional doping, such as a higher concentration of edge dislocation defects and a higher rotation of crystalline nanodomains in the plane of the films (normal to the preferential orientation c-axis) for the high content Al:ZnO layer. A complete description of such effects has been accomplished using several characterization techniques, such as X-ray diffraction, Raman spectroscopy and transmission electron microscopy. The combination of these techniques provides an exhaustive understanding of the films nanostructure.

DEPARTAMENTO DE FÍSICA APLICADA I
FACULTAD DE CIENCIAS
UNIVERSIDAD DE MÁLAGA

Fax: 952 13 23 82
29071 MÁLAGA (ESPAÑA)

Prof. P. Vincenzini
Editor
Ceramics International

Dear Professor Vicenzini,

We took the revision process very seriously and did thoroughly revise the original manuscript. We believe we fully addressed all of the reviewer's suggestions, including the one raised in his/her last report.

We respectfully believe that the reviewer's objections to that single sentence in the Conclusions of the revised manuscript are due to a mistake since the sentence, as cited by the reviewer, does not exist in the 2nd revised manuscript. The following is a screen capture (p. 25) of the revised manuscript:

Al:ZnO sample. This fact is compatible with a higher rotation of the crystallites in the *ab* plane, as ~~it is evident in~~ TEM planar view images seem to suggest for the high-Al:ZnO sample, respect to the low-Al:ZnO one.

And this is the text cited by the reviewer:

"This fact is compatible with a higher rotation of the crystallites in the ab plane, as it is evident in TEM planar view images seem to suggest for the high-Al:ZnO sample, respect to the low-Al:ZnO one"

Somehow, the text cited by the reviewer mixes both new text (added in blue color to address his/her initial suggestions) along with old deleted text, which had been struck through. Logically, the resulting text is meaningless, and would deserve the reviewer's objections and the editor's suggestion for language revision. But again, it was not the actual sentence in the 2nd revised manuscript, as shown by the image above which proves that we in deed addressed the reviewer's suggestion. However, we have decided to remove that sentence in order to fully satisfy the reviewer requirements.

We deeply regret this misunderstanding and would be grateful if you could consider the 3rd revised version of the manuscript for publication, as it addresses all of the reviewer's suggestions.

Thank you very much for your attention

Corresponding author:
Mercedes Gabás
Depto. Física Aplicada I, Lab. de Materiales & Superficies
Universidad de Málaga, 29071 Málaga (Spain)
Present address:
Instituto de Energía Solar
Universidad Politécnica de Madrid, 28040 Madrid, Spain
emails: mgabas@uma.es, mercedes.gabas@ies.upm.es

Answer to reviewer:

Reviewer #1: The paper reports on a deep investiagion of sputtered Al:ZnO films. Based on various characterization techniques the authors conclude that the Al is incorporated in the lattice on substitutional sites for Zn ions and the quality of crystallographic texture is deteriorated with high Al doping. The study is well organized and clearly described. The second revision clarifies all aspects.

I still disagree with the following statement in Conclusions section:

"This fact is compatible with a higher rotation of the crystallites in the ab plane, as it is evident in TEM planar view images seem to suggest for the high-Al:ZnO sample, respect to the low-Al:ZnO one."

Either you state you have more data or you cannot conclude like that. You do not need large statistics, but the data you provide are not sufficient to support such a statement. Too speculative. You mentioned in the replies to the reviewer you do not claim this anymore, but you still state this in conclusions. I suggest to mark it as speculation or expess a personal opinion of the authors, which is not sufficiently supported by the data.

We believe there has been a mistake since the sentence cited by the reviewer, does not exist in the revised manuscript. The following is a screen capture (p. 25) of the revised manuscript:

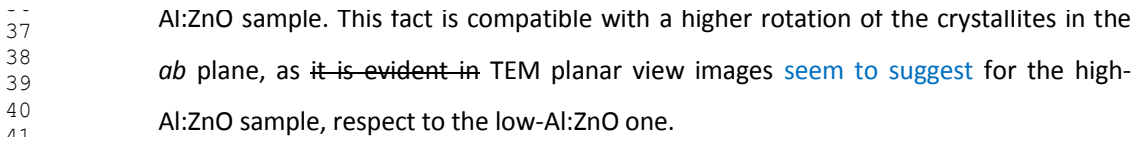
Al:ZnO sample. This fact is compatible with a higher rotation of the crystallites in the *ab* plane, as ~~it is evident in~~ TEM planar view images seem to suggest for the high-Al:ZnO sample, respect to the low-Al:ZnO one.

The sentence mentioned by the reviewer mixes both new text (added in blue color to address his/her initial suggestions) along with old deleted text, which had been struck through. Although we believe that the sentence shown in the screen capture addressed the reviewer's suggestion, we have removed it in the new revised version of our manuscript.

Nanostructural changes upon substitutional Al doping in ZnO sputtered films

A.R. Landa-Cánovas[1], J. Santiso[2], F. Agulló-Rueda[1], P. Herrero[1], E. Navarrete-Astorga[3], E. Ochoa-Martínez[3,4], J.R. Ramos-Barrado[3], M. Gabás[3,5]*

[1] Instituto de Ciencia de Materiales de Madrid (ICMM), CSIC, Cantoblanco, 28049 Madrid, Spain.

[2] Instituto Catalán de Nanociencia y Nanotechnología (ICN2), CSIC & BIST, Campus UAB, Bellaterra, Barcelona, Spain

[3]Dpto. de Física Aplicada I, Lab. de Materiales y Superficies,Universidad de Málaga, 29071 Málaga, Spain.

[4]Adolphe Merkle Institute, University of Fribourg, Chemin des Verdiers 4, 1700 Fribourg, Switzerland.

[5]Instituto de Energía Solar, Universidad Politécnica de Madrid, 28040 Madrid, Spain

Corresponding author:

Mercedes Gabás

Dpto. de Física Aplicada I, Lab. de Materiales y Superficies

Universidad de Málaga, 29071 Málaga, Spain.

Present adress:

Instituto de Energía Solar

Universidad Politécnica de Madrid, 28040 Madrid, Spain

e-mail: mgabas@uma.es; mercedes.gabas@ies.upm.es

ABSTRACT

Al:ZnO layers, with low and high Al content, 0.2% and 2.1% cat. respectively, have been prepared using the RF magnetron sputtering technique. Noticeable differences in the optical and electrical properties have been detected in these films. With doping, the resistivity decreases and the band-gap increases. The alterations in the films crystalline structure are explained in terms of the nanostructural changes induced by Al substitutional doping, such as a higher concentration of edge dislocation defects and a higher rotation of crystalline nanodomains in the plane of the films (normal to the preferential orientation *c*-axis) for the high content Al:ZnO layer. A complete description of such effects has been accomplished using several characterization techniques, such as X-ray diffraction, Raman spectroscopy and transmission electron microscopy. The combination of these techniques provides an exhaustive understanding of the films nanostructure.

Keywords: TCO; ZnO; Al doping; nanostructure

1. INTRODUCTION

Transparent conducting oxides (TCO) are a very important constituent in many optoelectronic devices. Among the materials that can fulfil the requirements for its incorporation in such devices (high enough conductivity and transmittance values, lightweight, cheap and compatible with large-scale manufacturing methods), doped ZnO has already become a proved alternative to traditional TCOs, such as indium-tin oxide (ITO) [1, 2]. The evolution of electro-optical properties of ZnO layers after doping with IIIA elements has been recently reported by several authors [3]. Among these, Al is the most popular due to its abundance and low cost. However, there is a limitation in the improvement of those properties when increasing dopant concentration above a certain value. For example, there are evidences of film conductivity saturation for an Al dopant content ~2% cat. – relative occupancy of Al in Zn sites- [4-6]. In that sense, Al-doping effects on the ZnO layer structure at the nanometric scale, and on the electronic levels on the proximity of band edges are still an issue that deserves much attention from the scientific community. There are some works that have paid attention to the Al distribution in the ZnO layer [7], or to the changes induced by Al in the ZnO electronic structure [8]. However, there are still many open questions concerning structural defects and nanostructural changes induced by Al doping, waiting for a suitable and convincing answer. The significant role that lattice defects have on the ZnO electronic structure and therefore their electro-optical properties has been reviewed recently by Wang et al. [9].

In a previous work, we analysed the optical behavior of sputtered Al:ZnO layers using spectroscopic ellipsometry [6]. Growth parameters were adjusted in order to obtain a wide range of Al content in the layers. The final purpose was to establish a relationship between the Al dopant content and the optical properties. In that work two different layer surface morphologies were observed, according to Al dopant content. For the low-doping layers (< 2% cationic content), the Al doped ZnO film optical behavior was very similar to that observed for an undoped ZnO film, while marked differences were detected for the films whose Al content was higher than 2% cat. Accordingly, the films resistivity exhibited a U-shaped behavior with a minimum value for the 2% cat. content film. This Al value seems to separate two different regimes. In the low-Al content

regime, opto-electronic properties are preserved or even improved with respect to the undoped ZnO, while the layer morphological characteristics are not much affected because of doping. In the high-Al content regime, a worsening of the electric conductivity is evident and noticeable changes affect layer morphology.

The aim of this work is to carefully study the nanostructure of undoped and Al-doped ZnO thin films. For such purpose low- and high-Al content doped films have been prepared in order to correlate the differences observed in the morphology and opto-electronic properties with structural changes induced by doping. The Al content in each film differs in one order of magnitude and the high-Al:ZnO film has just slightly surpassed the ~2% cat. content. Special care has been taken to attain just substitutional doping in this layer. The attempts to grow films with a larger Al content (>2% cat) resulted in formation of Al-containing secondary phases, which impeded the control over the substitutional Al content, and affected the remaining Al:ZnO structure. Therefore, an Al-content of about 2% was considered the effective solubility limit in this work. Therefore, the high-Al:ZnO film could be considered in the frontier between both regimes described in the preceding paragraph. The intention was to preserve the optimum opto-electronic properties of the doped films, and also, to prevent any structural alteration that could be ascribed to the possible formation of spurious phases apart from Al:ZnO.

Three different characterization techniques have been chosen in order to fully explore the structural alterations induced by doping in these ZnO layers. High resolution X-ray diffraction (HRXRD) is the basic tool that allows to achieve a full knowledge of the layer crystalline characteristics. On the other hand, by studying the lattice vibrations through Raman spectroscopy, we can extract valuable information concerning the symmetry, order, defects, chemical composition and bonding in the crystalline lattice. Finally, transmission electron microscopy (TEM) is very sensitive to local changes in the structure, facilitating thus the interpretation of the subtle effects that the existence of extended defects, or any other structural alteration due to the introduction of Al dopant in the ZnO structure, can produce. Therefore, it provides complementary information to the one obtained by the other structural characterization techniques, HRXRD and Raman spectroscopy.

2. EXPERIMENTAL

The ZnO and Al:ZnO films were deposited on p-type Si (001) and silica substrates by RF magnetron sputtering. Two types of ceramic targets from AJA International Inc. were employed simultaneously: ZnO (99.99%) and Al_2O_3 (99.9%). Dopant content was modulated by the power supplied to the Al_2O_3 target, 20 W (low-Al doping) and 55 W (high-Al doping), while for the ZnO target the power was always set to 150W. The working pressure into the vacuum chamber was maintained at 1.4 x 10^{-2} mbar with a high purity (5.0) Ar gas, regulated by a mass flow controller at 12 sccm. The substrate temperature was maintained constant at 300°C, and all the samples were deposited during 20 minutes, except for much thicker samples measured using Raman spectroscopy, that were deposited for 3 hours. Estimated thickness for these last films is between 600 and 700 nm [10].

Secondary neutral mass spectrometry (SNMS) has been used to determine the [Al]/[Zn] ratio by means of a INA-X, SPECS GmbH, in high frequency mode (HFM) by using Ar^+ ions with a fairly low energy for sputtering (E_{Ar+} = 200 eV). SEM images were acquired in a Helios Nanolab 650 dual beam SEM-FIB from FEI. The optical transmittance of the films grown onto quartz substrates was measured using a UV-vis spectrophotometer (Varian Cary 5000) in the wavelength range 250-2500 nm. The dielectric response of the layers was characterized in a Semilab GES-5E variable angle spectroscopic ellipsometer in the wavelength region from 233 to 1700 nm (photon energies of approximately 5.3 to 0.73 eV) at room temperature. A microspot configuration with a spot size of approximately 400 μm and an angular aperture of 4.25 degrees was used. The incident and analyser angles have been set fixed at 75 degrees. The resulting spectra were fitted with SEA software. A four points device has been used to measure the resistivity of the films. The setup consists in a Faraday isolation cage (Hewlett-Packard 16055), a Picoamperimeter/nanovoltmeter (Keithley 181), a DC power supply and an analyser (Keithley 2400).

The X-ray diffraction scans were carried out in a X'Pert Pro (from PANalytical) diffractometer with CuKα radiation. Out-of-plane parameters and crystal domain orientation distribution were extracted from standard (Bragg-Brentano geometry) 2θ-

ω scans and rocking curves (ω scans), while in-plane cell parameters were determined from grazing incidence and grazing diffracted geometry (in-plane diffraction).

Raman spectra were measured with a Renishaw Ramascope 2000 system. A He-Ne laser (emission wavelength 632.8 nm) was used for excitation. Light was focused on the sample with a 100× microscope objective and collected in backscattering geometry. The probing depth (about 2 μm) was larger than the ZnO film thickness and therefore the Raman spectra contain also a large contribution from the substrate material. To reduce the disturbance from the latter, films for the Raman experiments were deposited on silica glass, which has a weaker and broader Raman spectrum than the silicon substrates used for the other samples.

Plane-view and cross-sectional samples were prepared for the TEM study. Plane view samples were prepared by dimple-grinding with a Gatan 656 dimpler and ion-milling with a Fischione 1010 model. Cross-sectional samples were prepared using the Helios Nanolab 650 dual beam SEM-FIB from FEI. Both types of samples have been characterized by TEM using a JEOL 3000F transmission electron microscope with a field-emission gun, 300 kV acceleration voltage and with 0.17 nm point resolution for high resolution TEM (HRTEM).

3. RESULTS

A basic characterisation of the films, including optical and electrical behaviour, as well as a quantification of the dopant content along the film thickness, was first accomplished to ensure its suitability as potential TCOs. The main results are gathered in Table 1. Accordingly to SNMS experimental results, [Al]/[Zn] ratio differs by one order of magnitude between the less and the more doped films.

The optical properties of the films have been studied through transmittance and spectroscopic ellipsometry measurements. Layers studied using these techniques were grown at the same time on different substrates: silica for the transmittance measurements and p-type silicon (100) for the ellipsometry analysis. Different substrates do not alter layer properties, as we previously observed in some other ZnO

films [10, 11]. The first technique allows to explore the films transparency in the visible range, which is a fundamental property in a TCO. For these samples, the transmittance values are over 85% along the whole visible range, reaching values of 87.5% (ZnO), 85.5% (low-Al) and 88.0% (high-Al) at 555 nm (not shown). To obtain the band-gap by transmittance measurements, we have plotted $(\alpha h\nu)^2$ vs. $h\nu$, where α is the absorbance calculated as [ln(1/transmittance)]/thickness, h the Planck constant (4.13×10^{-15} eV s^{-1}) and ν the frequency (speed of light/wavelength). Then, the intersection of the curves with the X-axis (slope of the curves) corresponds to the band-gap. Experimental band-gap values are 3.2(2) eV for the undoped and the low-Al doped ZnO films, while it reaches 3.5(2) eV for the high Al-doped ZnO film. Transmittance measurements have verified the effective band-gap enlargement due to substitutional doping caused by the filling of the states at the bottom of the conduction band (Burstein-Moss effect) [12]. However, the doping-induced stress on Al-ZnO films could be an additional reason for the blue-shift observed in the band-gap [13].

The dependence of optical properties with doping in this type of Al:ZnO films has been recently studied using spectroscopic ellipsometry, with only one mathematical model being able to describe the dielectric function behavior along a wide wavelength region [6]. In the present work, the films optical response is also explained using such a model. As in the above mentioned work, there are noticeable differences in the complex refractive index between the undoped and the low-Al doped ZnO films on one hand, and the high-Al doped ZnO film, on the other hand (Figure 1). A clear Burstein-Moss shift is observed in the absorption coefficient of the last sample, as compared to the undoped and the low-Al doped ZnO films. The refractive index main peak evidences an intensity decrease associated with a broadening increase, which can be explained by electrostatic screening due to free electrons excess in the high-Al doped film [12]. Our ellipsometry results agree with the band-gap displacement after Al-doping observed for the transmittance measurements.

The films resistivity has been measured using the Van der Pauw method on samples prepared onto silica substrates, in order to prevent substrate contribution to the film conductivity. As expected after substitutional doping, a significant decrease on the film

resistivity values has been detected, two orders of magnitude for the low-Al film and almost five orders for the high-Al film.

Table 1: Electro-optical parameters of the three studied samples.

	ZnO	low-Al	high-Al
[Al]/[Zn] ratio		0.2	2.1
% transmittance at 555 nm	87.5	85.5	88.0
Band-gap (transmittance) (eV)	3.2(2)	3.2(2)	3.5(2)
Band-gap (ellipsometry) (eV)	3.1(8)	3.2(2)	3.5(6)
Resistivity (Ω×cm)	$4.6(9)\times10^{2}$	5.8(8)	$4.1(5)\times10^{-3}$

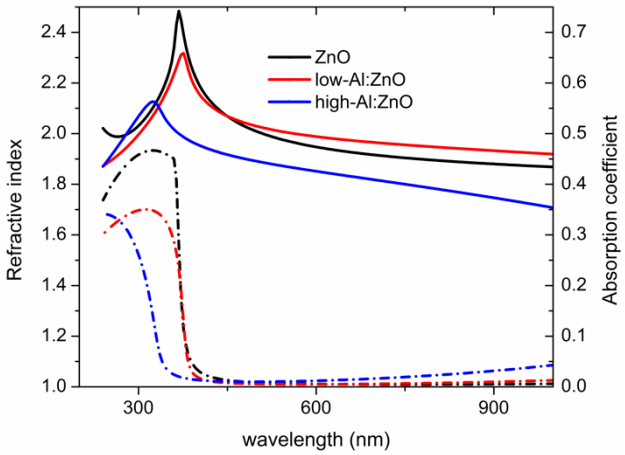

Figure 1: Complex refractive index of the ZnO and Al:ZnO films. Solid lines: refractive indexes; dashed-dot lines: absorption coefficients.

The films surface morphology has been checked using SEM micrographs (Figure 2), demonstrating the changes induced in the high-Al content doped film. The undoped film surface (not shown here) appears very similar to that of the low-Al content doped film, showing a pinnacle shape termination of the columns arranged in the layer. The high-Al content film exhibits a different surface appearance, very similar to that shown for films with an Al content higher than 2% cat. [6].

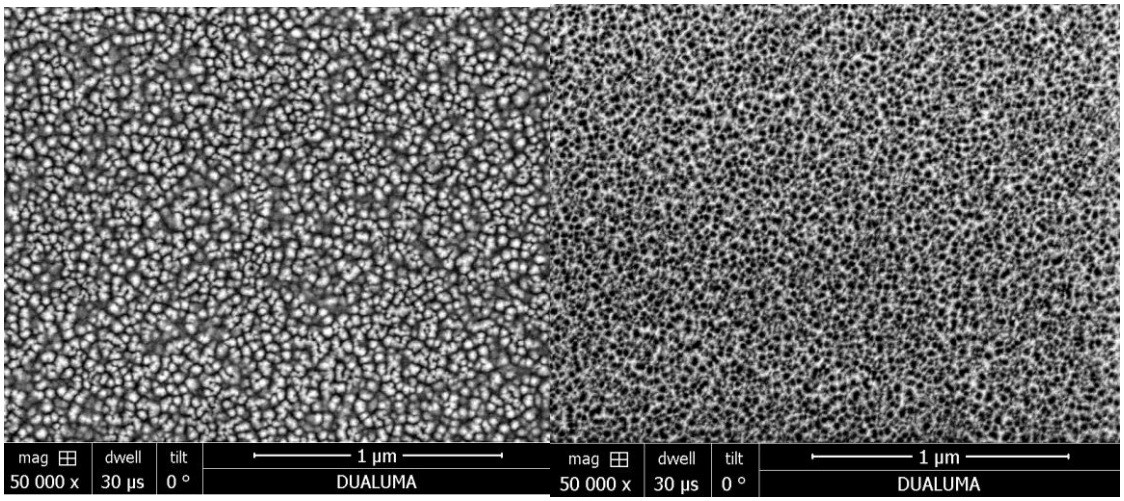

Figure 2: left, SEM planar view corresponding to the low-Al content ZnO doped film; right, ibid for the high-Al content ZnO doped film.

After this basic characterization, it can be concluded that, in spite of the very small Al amount in the low-Al:ZnO sample, layer conductivity gets improved by two orders of magnitude, demonstrating thus the important effects that n-doping is able to induce in these transparent oxides. The high-Al:ZnO sample is probably on the verge of the dopant efficiency in these layers. It keeps a good transmittance value and exhibits very high conductivity, but its surface morphology suggests it is on the vertex of the U-shaped curve which relates resistivity vs. dopant content for these Al:ZnO layers [4-6].

3.1 HRXRD characterisation

The undoped ZnO film served as a reference of the ZnO with wurzite structure. Figure 3 shows the complete 2θ scans for the three samples showing basically ZnO(00ℓ) ℓ = 2, 4 and 6 reflections, along with intense Si substrate peaks. No trace of $ZnAl_2O_4$ spinel structure was observed. The appearance of only 00ℓ peaks indicate the pure *c*-axis orientation of the films, as it has been observed repeatedly in some other doped ZnO films prepared under similar growth conditions [6, 10, 11].

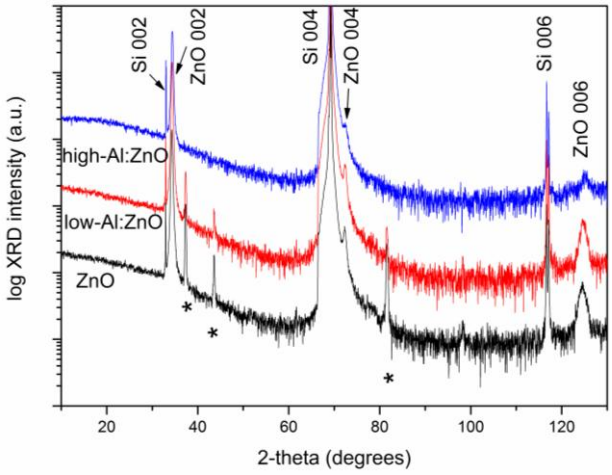

*Figure 3. X-ray diffraction 2θ scan of the sputtered ZnO films with different Al content. The peaks indicated with an asterisk * correspond to a sample holder impurity and not to the sample. Curves corresponding to different samples have been vertically shifted for clarity.*

A zoom of the ZnO(002) area is depicted in Figure 4. It is clear from the position of the peaks that the incorporation of Al into the structure produces a shift towards higher angle, which corresponds to a subtle *c*-axis reduction from *c* = 5.2248±0.0005 Å in the undoped ZnO film, to *c* = 5.2205±0.0005 Å for the high-Al sample. Although this is a very small reduction of about -0.08%, it is still significant given the accuracy of the cell parameter determination by HRXRD. This cell parameter reduction is consistent with the expected trend due to the smaller size of the Al^{3+}cations acting as substitutional dopants in the Zn^{2+} positions. Ionic radii for Al^{3+} and Zn^{2+}, in tetrahedral coordination are *r* = 0.53 Å and *r* = 0.74 Å, respectively, (as extracted from crystal radii in [14] assuming $r(O^{2-})$ = 1.26 Å).

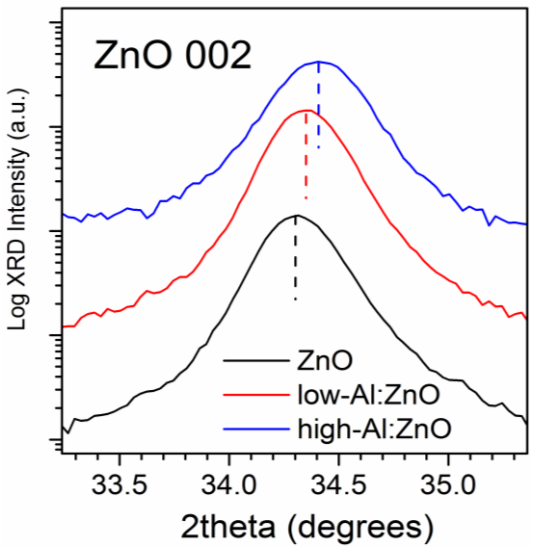

Figure 4. Detail of the 002 ZnO reflection for the three samples. Curves corresponding to different samples have been vertically shifted for clarity.

The differences in the 002 ZnO reflection width in the 2θ scan, as well as some other structural parameters, are gathered in Table 2. The 2θ peak width is directly related to the crystal quality in the vertical direction, while the broadening of the rocking curve corresponds to the overall orientation distribution of the crystallites around the growth direction. The low-Al:ZnO sample does not seem too different from the undoped ZnO sample. This indicates that the crystal quality as well as the preferential orientation of the crystallites are preserved for small Al content. The 2θ peak broadening shown in the high-Al sample indicates a larger distribution of cell parameter values along the growth direction. The concomitant broadening of the rocking curve (ω scan at fixed 2θ) for the high-Al sample, about twice the value than for the undoped and low-Al samples, indicates a perturbation of the layer growth habit, with a larger distribution of crystallite orientations around *c*-axis.

Table 2: Structural parameters deduced from 002, 100 and 110 reflections for the three studied samples.

	ZnO	low-Al	high-Al
[Al]/[Zn] ratio		0.2 %	2.1 %
c-parameter (Å)	5.2248±0.0005	5.2233±0.0005	5.2205±0.0005
FWHM 002 reflection (degrees)	0.336	0.326	0.393
Rocking curve FWHM (degrees)	2.24	2.40	4.47
a-parameter (Å) 100 reflection	3.2399±0.0005	3.2434±0.0005	3.2391±0.0005
a-parameter (Å) 110 reflection	3.242±0.001	3.247±0.001	3.239±0.001

In order to distinguish whether the observed *c*-parameter reduction for the high-Al:ZnO layer is an effect of the substitutional Al, or it is due to a possible variation in the residual strain due to some microstructure changes, we carried out in-plane cell parameters determination by XRD using the in-plane geometry. In this geometry grazing incidence and diffracted beams (ω=0.5°) are used, and therefore only the planes which are strictly perpendicular to the film surface give rise to diffraction peaks. In this case, the most intense 100 and 110 reflections were analysed for the three different samples as depicted in Fig. 5. The corresponding cell parameters (Table 2) were extracted from the peak positions. The in-plane *a*-parameter was directly determined from the 100 and 110 reflections, assuming $\frac{1}{d_{hkl}^2} = \frac{4}{3}\frac{h^2+hk+k^2}{a^2} + \frac{l^2}{c^2}$ for an hexagonal structure. In this case $a = \frac{2}{\sqrt{3}} d_{100}$ and $a = 2d_{110}$.

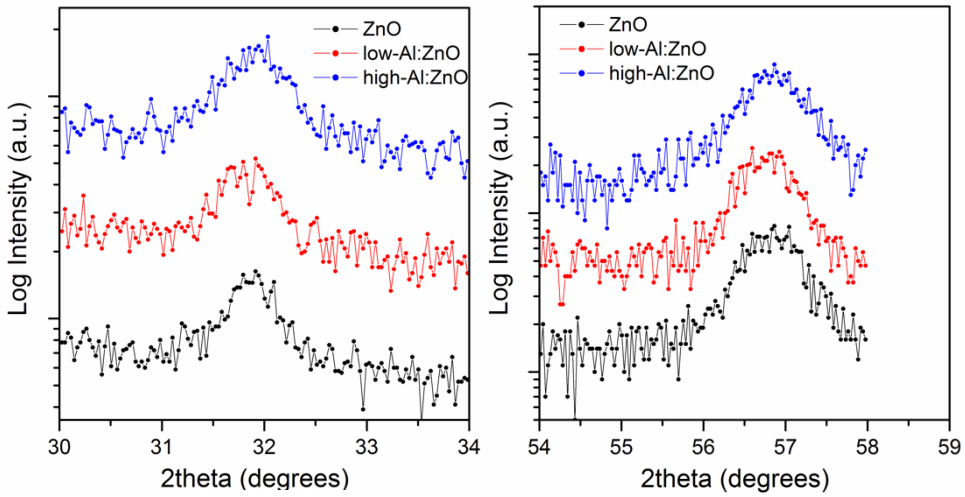

Figure 5. In-plane geometry 2θ scans of 100 (left) and 110 (right) film reflections. Curves corresponding to different samples have been vertically shifted for clarity.

Despite the large error in the cell parameter determination, inherent to the large peak broadening at the in-plane geometry, the *a*-parameter is reduced in the high-Al sample, as compared to the low-Al one. This implies, along with the observed reduction in *c*-parameter, that the overall cell volume becomes smaller. The presence of an in-plane biaxial strain induced by the different thermal expansion of film (2.49×10^{-6} K^{-1} and 4.26×10^{-6} K^{-1} at 300K and 700K, respectively [15]), and substrate (2.63×10^{-6} K^{-1} and 4.00×10^{-6} K^{-1} at 300K and 700K, respectively [16]) would have produced an opposite elastic response in out-of-plane and in-plane cell parameters, thus compensating for cell volume changes. Therefore, the cell volume reduction upon increasing Al target power is consistent with the incorporation of Al^{3+} in the Zn^{2+} sites of the ZnO wurzite structure, rather than to the relaxation of any residual strain produced during growth.

3.2 Raman spectroscopy characterization

The Raman spectra of the Al:ZnO films deposited on silica glass substrates are shown in Figure 6. For a perfect wurtzite crystal (space group of symmetry $P6_3mc \equiv C_{6v}^4$, $Z = 2$) group theory predicts 6 Raman active peaks with symmetries A_1(TO) + A_1(LO) + E_1(TO)

+ E_1(LO) + 2 E_2, where the LO-TO splitting of the polar modes has been considered [17]. The Raman peaks are labeled in Figure 6 with the assigned symmetry species. Because the films are much thinner than the depth resolution of the Raman microscope, the original spectra have an important signal from the substrate. Thus the spectrum of a bare substrate has been subtracted from the original spectra in order to get the spectra of the ZnO films alone.

For the low-Al:ZnO sample, the strongest peaks correspond to the E_2(low) and the E_2(high) modes at 99 and 435 cm^{-1}, respectively. A weaker peak is observed at 582cm^{-1}. For Raman backscattering along the ZnO crystal *c* axis, the only modes allowed are the two E_2 modes and the A_1(LO) mode at 574 cm^{-1} [17]. However, the latter mode is very weak in an undoped crystal [18]. Therefore, the most reliable explanation for the band at 582 cm^{-1} is that it is mostly due to the E_1(LO) mode that, although forbidden in backscattering for a perfect crystal, is activated by the electric field at the surface of the ZnO nanocolumns [19]. The shoulder on the low energy side can be due to the A_1(LO) mode [14], to the defect activated B_1(high) mode [20], or to free carriers [21]. In any case the strength of the E_2 modes relative to the TO modes confirms that the film is oriented with the *c* axis along the growth direction, in agreement with the XRD results. Several other peaks, much weaker than the ones discussed above, can be clearly seen in the spectrum. The peak at 378 cm^{-1} is the A_1(TO) mode, which is forbidden in backscattering along the *c* axis, but can appear because of some deviation of the *c* axis of the nanocolumns with respect to the normal to the interface plane. The B_1(low) phonon is Raman inactive in a perfect wurtzite crystal but becomes active after doping because of the impurity-induced breaking of translational symmetry [20]. The peak at 330 cm^{-1} has been attributed to E_2(high)–E_2(low) second order mode [22].

For the high-Al:ZnO sample the Raman spectrum shows smeared out bands, indicating a larger disordering of the crystal lattice and the presence of free carriers. The A_1(TO) peak becomes more intense, indicating a larger misorientation of the columns along the *c* axis. This conclusion is compatible with the XRD results, where the 002 reflection peak broadening for the high-Al:ZnO sample indicates a larger distribution of the *c* axis cell parameter along the growth direction. Also, a very broad band becomes apparent

at around 500 cm^{-1}. This band has tentatively been attributed to free carriers in highly Al doped ZnO [21]. In that sense, the Raman spectra are in accordance with the changes detected in the layer optical and electrical properties, when comparing resistivity and band-gap values of the high- and the low-Al:ZnO samples.

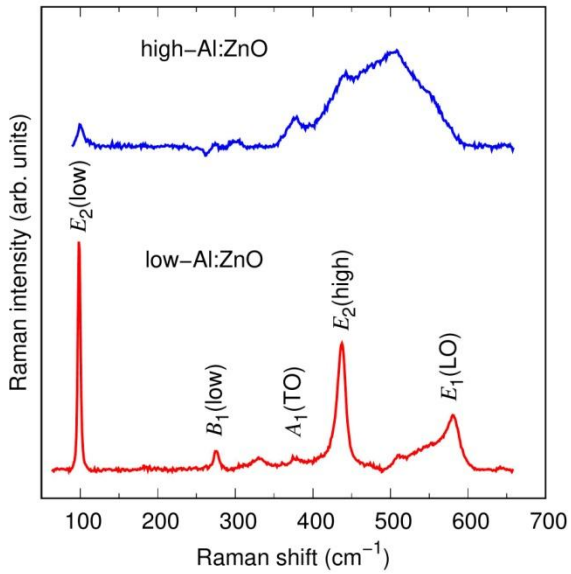

Figure 6: Raman spectra for the Al:ZnO films grown on a silica glass substrate. The contribution from the silica substrate has been subtracted. Spectra have been vertically offset for clarity. Laser wavelength was 632.8 nm.

3.3 TEM characterization

TEM observation of the cross-section of low-Al:ZnO sample shows an Al:ZnO layer of prismatic crystals 60-70 nm long along the ZnO *c*-axis, see Fig. 7 top left. The Fast Fourier Transform (FFT) of the layer image is indexed as ZnO hexagonal structure and it shows that the layer is oriented along the [100] zone axis with the *c* axis perpendicular to the Si-ZnO interface, in concordance with XRD and Raman spectroscopy results (Inset in Fig. 7 top right). However, the crystal boundaries are not as well defined as in the case of pure ZnO sample [10], showing less crystalline habits. Therefore, it is not easy to determine the crystal edges in the *ab* plane. The high resolution image of the

cross section, see Fig. 7 top right, shows the (0002) lattice planes running almost continuously parallel to the Si-ZnO interface. In well aligned crystals, a two dimensional image is observed thanks to the contribution of 01-10 reflections. Besides, in the same areas, a double periodicity along c* can be seen due to the weak 0001 reflections, see the FFT in Fig. 7 top left**.** These reflections are forbidden and appear due to the dynamical nature of electron scattering. When the crystal is slightly misaligned the conditions that allow the transfer of intensity to the forbidden reflections disappear, in such way, only the basic lattice fringes of the (0002) lattice planes are observed. Edge dislocation defects are common as it can be observed in the HRTEM image of Fig. 7 top right. The processed image of HRTEM image of Fig. 7, by filtering the 002 (ZnO) reflections to reconstruct the image, shows more clearly the dislocations (see Fig. 7 bottom left). We have also added a blow up of one of the dislocations and shown the determination of the Burgers vector **b** = 1/2 c_{ZnO} (Fig. 7 bottom right). They are probably the origin that gives rise to the A_1(TO) forbidden mode detected in the Raman spectra at 378 cm^{-1} (Figure 6).

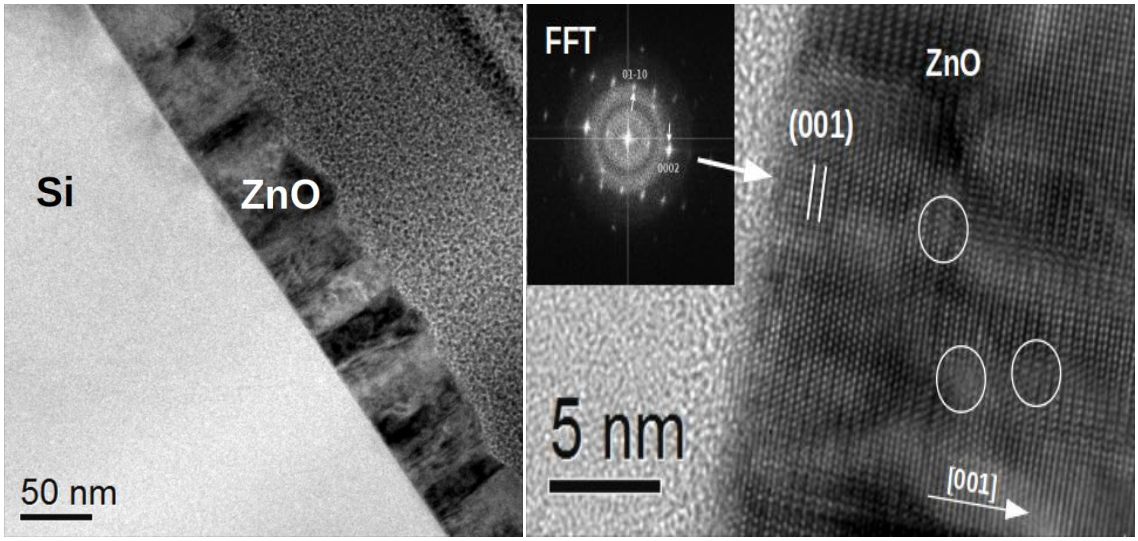

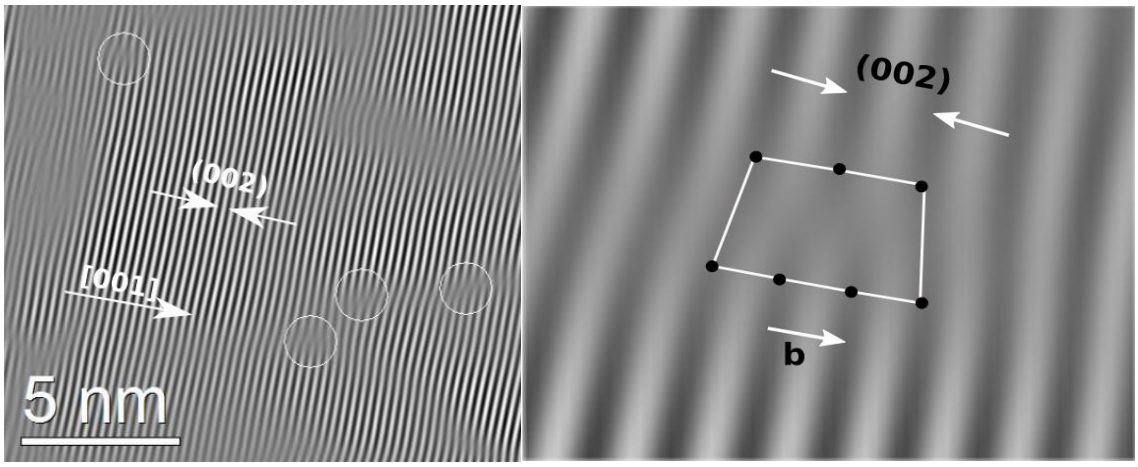

Figure 7. Top left: low magnification TEM image showing the low-Al:ZnO layer (center) and the Si layer (left). Top right: HRTEM image of the Si-ZnO interface oriented along the ZnO [100] zone axis. The silicon layer is on the left side, ZnO on the right side. Edge dislocations are indicated with white circumferences. Inserted is the FFT of the ZnO layer HRTEM image. An arrow is drawn to show that the 00l reflections row of the FFT is perpendicular to the interface and to the (001) lattice planes, also drawn in the HRTEM image. Bottom left: processed image from the HRTEM image filtered using the 002 reflections. Bottom right: blow up of one dislocation showing the determination of the Burgers vector $\boldsymbol{b} = 1/2\ \boldsymbol{c}_{ZnO}$.

The TEM images of plane-view prepared samples are more useful to determine the particle size in the *ab* plane than the cross-section images, since they present very well defined and crystalline ZnO crystals, see Fig. 8 top. The ZnO crystallites range between 5 and 10 nm in diameter. The crystals images are dominated by Moiré fringes due to the superposition of Si and ZnO lattice fringes. The selected area electron diffraction (SAED) patterns seem quite complicated, see Fig. 8 middle, but can be easily understood as produced by multiple diffraction phenomena between the silicon and the ZnO layers, see the schematic drawing of Fig. 8 bottom. The diffraction rings are produced by random oriented ZnO nanocrystallites. Only *hk0* diffracted rings have been indexed so, although the ZnO crystallites are randomly rotated, they are all oriented with the *c* axis perpendicular to the ZnO-Si interface. In the same diagram the single crystal *hk0* sharp diffraction maxima from silicon can also be observed. Each silicon diffraction maxima have been coloured in a different colour. Being the sample a plane view preparation, i.e., the sample has been thinned parallel to the Si-ZnO interface, it occurs that in moderately thick areas of the sample, both ZnO and Si

signals superimpose. Therefore, due to the dynamic nature of electron diffraction, electron beams scattered by the silicon layer cross the polycrystalline ZnO layer and diffract again. That phenomenon produces a set of diffraction rings around each silicon diffracted spot that have been coloured in the same colour as the original Si reflection in the scheme of Fig. 8 bottom. The superposition of the original silicon single crystal diffraction pattern, with the original ZnO polycrystalline pattern and the double-diffraction rings around each silicon maxima, gives rise to the complicated pattern of Fig. 8 bottom.

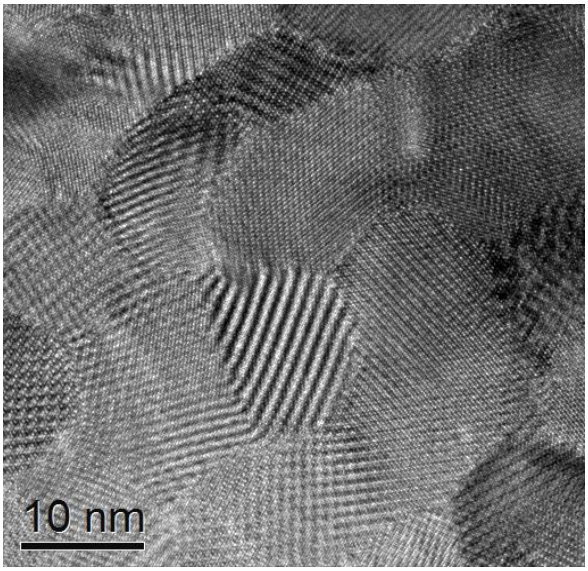

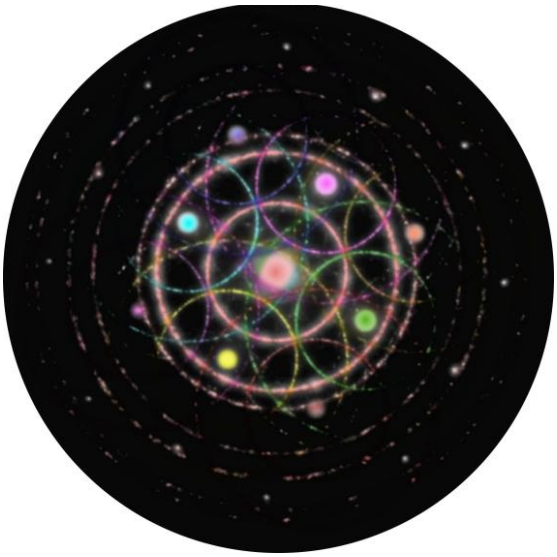

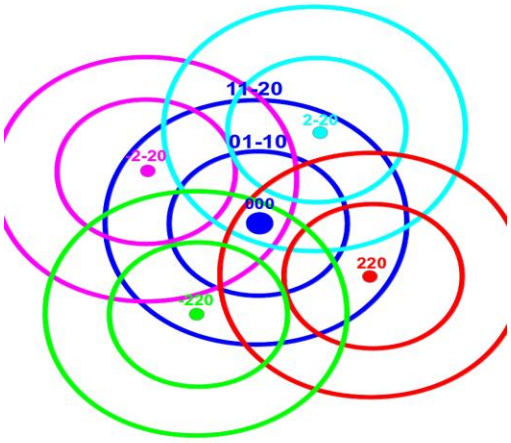

Figure 8. Top, HRTEM image of a plane-view low-Al:ZnO sample showing nanodomains. Moiré fringes are due to the interaction between Si and ZnO lattice planes. Middle, SAED pattern of a plane view sample with colours added artificially. Bottom, simplified scheme of the diffraction pattern shown in middle figure. Each silicon diffraction maxima has a different colour and the diffraction rings generated from them by double diffraction are coloured in the same colour.

Both the electron diffraction patterns and the TEM images suggest that the ZnO crystals are randomly oriented in the *ab* plane. However, when we study at higher magnification isolated ZnO crystals closer to the sample edge, without the silicon layer underneath, we obtain the image presented in Fig. 9 top, where three nanoparticles can be clearly distinguished. The FFTs corresponding to these three nanoparticles are presented in Fig. 9 bottom. All of the nanocrystallites are oriented along the [001] zone axis and the FFTs show that each particle is rotated respect to its neighbour particle. When doing SAED in the area shown in Fig. 8 top, many particles contributed to the diffraction pattern (those collected under the selected diffraction aperture), and

statistically they are randomly distributed but oriented on the [001] zone axis, giving rise to the diffraction rings seen in Fig. 8 bottom. Each particle is rotated respect to its neighbour particle ca. ~10º, as HRTEM image and SAED patterns in Fig. 9 show. These values are similar to those reported by Kohl et al. [23]. This finding is in agreement with the similar values of the 002 reflection FWHM rocking curve obtained for the undoped and the low-Al:ZnO layer (Table 2). Notice as well that the grain borders do not present a strong contrast indicating that there is not a big strain between the particles.

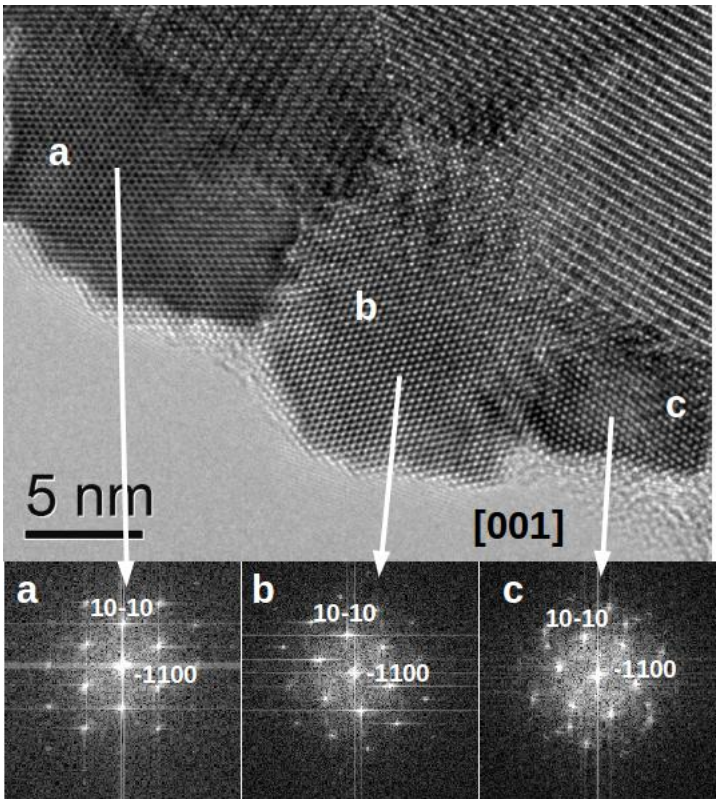

Figure 9: Top, HRTEM image of a plane view from low-Al:ZnO nanocrystals at the edge of the hole made by ion-beam thinning of the sample. Bottom, FFTs from the three ZnO nanocrystallites labelled as a, b and c, showing rotated [001] ZnO zone axis.

The TEM study of the high-Al:ZnO sample presents some differences with the low-Al:ZnO sample. The cross section preparation of this sample presents a layer of prismatic crystals of ZnO of 60-70 nm along *c* on top of a silicon layer (Fig. 10 top), very

similar to the previous sample. In the *ab* plane it is more difficult to establish the ZnO particle size due to the lack of contrast of the crystallite edges. These crystallites seem to be even less prismatic than in the case of low-Al:ZnO films (Figure 7 top right). The HRTEM image show an amorphous layer of SiO_2 in the ZnO-Si interface as it was already observed in previous works [10, 11]. Notice as well the big amount of edge dislocations with the same Burgers vector as in Fig. 7, i.e. $\boldsymbol{b} = 1/2\ \boldsymbol{c}_{ZnO}$. The filtered image in Fig. 10 bottom allows to estimate that in this high-Al:ZnO sample, the amount of edge dislocations is much bigger than in the low-Al:ZnO sample. This image has been processed from the FFT of the HRTEM image, then filtering the 0002 and 000-2 reflections and reconstructing the image with an inverse FFT. Now, with only the contribution of the 0002 reflections in the image, it is easier to see the edge dislocations which have been marked with red circumferences. This abundance of dislocations suggests the idea that the size of the crystallites observed by HRTEM (Fig. 10 top) could be on the order of 2-3 nm in the *ab* plane. Besides, it is probably responsible of both, the 002 reflection FWHM increase (Table 2), and the enhanced intensity of the A_1(TO) mode in the Raman spectrum (Figure 6), observed for the high-Al:ZnO sample in comparison with the low-Al:ZnO one.

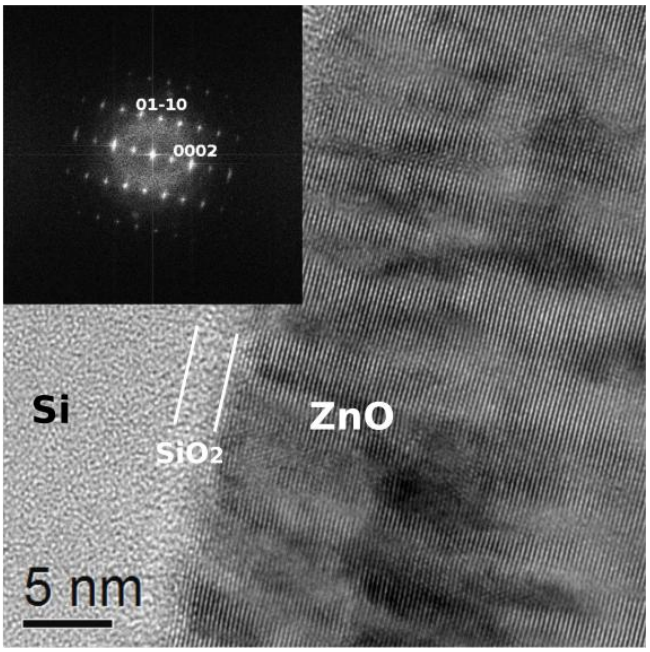

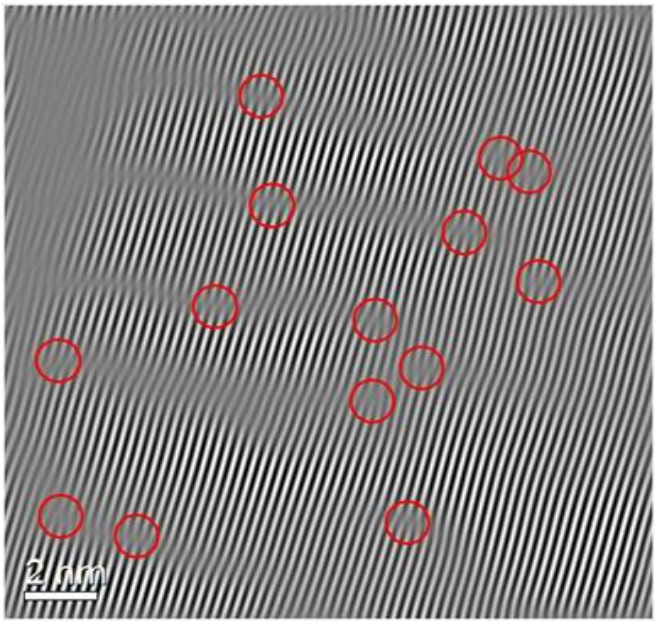

Figure 10. Top, HRTEM image of Si-ZnO interface in a cross section of high-Al:ZnO sample. The silicon layer is on the left side, ZnO on the right side. Inserted is the ZnO layer FFT oriented along [100] zone axis. Besides, a great number of edge dislocations are observed in the ZnO layer. Bottom, processed image of the ZnO area of the HRTEM image. Edge dislocations have been marked with red circumferences.

When the sample is observed perpendicular to the [001] ZnO direction, i.e., when we study plane-view preparations by TEM (Fig. 11 top), we see much bigger crystals than in the cross-section observations. The crystals range now between 20-30 nm, bigger than in the low-Al:ZnO sample. The HRTEM image is shown in Figure 11 middle, showing very good quality crystals, in contrast to what is suggested in the cross section image, with a high concentration of edge dislocation defects. In this HRTEM image this kind of defect is undetectable because its Burgers vector is along the *c* axis, and they are then invisible along the [001] direction. The crystallites very often share triple points and the grain boundaries are very well defined. Notice that now the grain boundaries present a very strong contrast, more intense that the observed in the low-Al:ZnO sample. The corresponding FFTs of the three particles in middle image are at

the bottom of the figure. These FFT´s show that each particle is clearly rotated around [001] direction respect to the nearest neighbour-being ~ +9º the rotation of particle b respect to particle a and ~ -19º the rotation of particle c respect to particle a. In this case, rotation of the crystals seems to produce a large structural strain in the grain boundaries between the particles, giving rise to the strong contrast that we observe in the HRTEM images. This observation agrees with the XRD conclusions deduced from the 002 rocking curve FWHM widening for the high Al:ZnO sample. This, together with the high concentration of dislocation defects observed in the cross section image (Figure 10) confirms the average structural differences between the low-Al and high-Al samples observed in HRXRD.

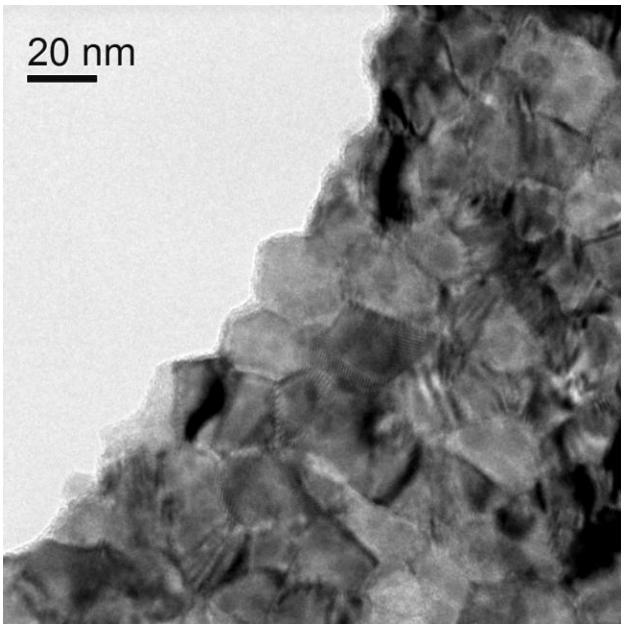

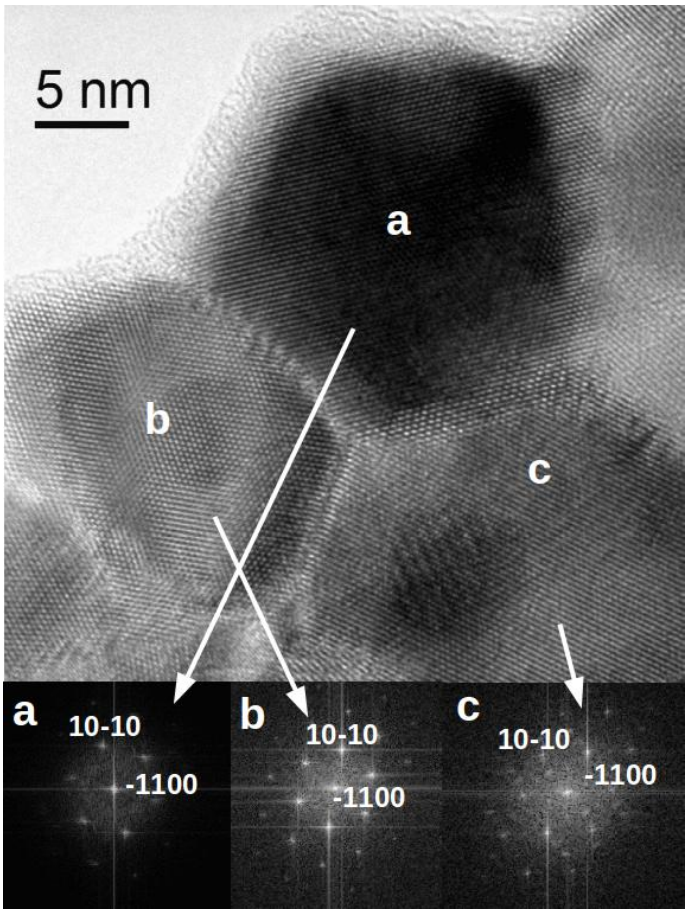

Figure 11: Top Low magnification TEM image of a plane view preparation of the high-Al:ZnO sample. Middle, HRTEM image showing three ZnO nanocrystallites with a common triple point. Bottom, FFTs from the three ZnO nanocrystallites labelled as a, b and c, showing rotated [001] ZnO zone axis

4. CONCLUSIONS

Al doped ZnO sputtered layers have been carefully analysed in order to explore the changes induced in the film microstructure after doping. The low-Al:ZnO sample optical properties are quite similar to that of the undoped material, while the electrical behaviour shows a reduction in the film resistivity. The high-Al:ZnO sample evidences noticeable changes in both resistivity and band-gap values, compatible with an excess of free carriers provoked by substitutional doping. This is also behind the broad signal at 500 cm^{-1} in the Raman spectrum corresponding to high-Al:ZnO sample. In spite of

doping, all the films retain the characteristic growth habit along *c* axis, as it is evidenced in XRD patterns, Raman spectra and TEM cross-section images. The XRD technique has demonstrated that Al atoms are included as substitutional dopants in these sputtered ZnO layers, as it is confirmed by the reduction of both, *a* and *c* parameters. HRTEM planar-view images show very crystalline and ordered nanodomains for both samples although crystal sizes are different.

For the low-Al:ZnO sample, the 002 reflection FWHM is comparable to that of undoped ZnO, while it increases for the high-Al:ZnO sample. That would indicate that crystalline quality along the growth direction, *c* axis, is maintained for low Al doping, but it gets worse as Al content in the layer increases. Accordingly, the worsening of the layer crystallinity along *c* axis, as the amount of dopant in the layer increases, is the origin of the A_1(TO) mode, forbidden in backscattering for a perfect ZnO crystal. This mode intensity is enhanced in the high-Al:ZnO sample as compared to the low-Al:ZnO sample. The nanostructural origin of these macroscopic differences could originate on the higher concentration of edge dislocation defects observed for the high-Al:ZnO in TEM cross-section images.

Concerning the 002 reflection rocking curve FWHM, it shows a clear increase with doping, which suggests a marked crystallite misorientation in the *ab* plane for the high-Al:ZnO sample.

The combination of the three techniques, XRD, Raman spectroscopy and TEM, has allowed to identify the nanostructural modifications that produce the changes observed in the optical and electric properties of these ZnO layers after substitutional Al doping.

Acknowledgments

This work was co-financed by MINECO projects MAT2014-57547-R, TEC2014-53906, MAT2016-77100-C2-1-P, and grant no. SEV-2013-0295 and the AGAUR agency for 2017SGR. Technical support from Mª Jesús Castelo (Univ. Carlos III, Madrid, Spain) in the preparation of plane view TEM samples is gratefully acknowledged.

REFERENCES

[1] D.S. Ginley, H. Hosono, D.C. Paine, Handbook of Transparent Conductors, Springer, New York, 2010.

[2] Ü. Özgür, D. Hofstetter, H. Morkoc, ZnO devices and applications: a review of current status and future prospects, Proc. IEEE 98 (2010) 1255–1268.

[3] K. Ellmer, A. Bikowski, Intrinsic and extrinsic doping of ZnO and ZnO alloys, J. Phys. D: Appl. Phys. 49 (2016) 413002.

[4] T. Minami, H. Sato, H. Nanto, S. Takata, Group III impurity doped zinc oxide thin films prepared by RF magnetron sputtering, Jpn. J. Appl. Phys. 24 (1985) L781–L784.

[5] I. Valenti, S. Benedetti, A. di Bona, V. Lollobrigida, A. Perucchi, P. Di Pietro, S.Lupi, S. Valeri, P. Torelli, Electrical, optical, and electronic properties of Al:ZnO films in a wide doping range**,**J. Appl. Phys. 118 (2015) 165304.

[6] E. Ochoa-Martínez, E. Navarrete-Astorga, J.R. Ramos-Barrado, M. Gabás, Evolution of Al:ZnO optical response as a function of doping level, Appl. Surf. Sci. 421 (2017) 680-686.

[7] A. Bikowski, M. Rengachari, M. Nie, N. Wanderka, P. Stender, G. Schmitz, K. Ellmer, Research Update: Inhomogeneous aluminium dopant distribution in magnetron sputtered ZnO:Al thin films and its influence on their electrical properties, Appl. Phys. Lett. Mater. 3 (2015) 060701.

[8] W. H. Huang, S. J. Sun, J. W. Chiou, H. Chou, T. S. Chan, H.-J. Lin, K. Kumar, J.-H. Guo, Electronic structure of Al-doped ZnO transparent conductive thin films studied by x-ray absorption and emission spectroscopies, J. Appl. Phys. 110 (2011) 103705.

[9] J. Wang, R. Chen, L. Xiang, S. Komarneni, Synthesis, properties and applications of ZnO nanomaterials with oxygen vacancies: A review, Ceram. Int. 44 (2018) 7357–7377.

[10] M. Gabás, P. Díaz-Carrasco, F. Agulló-Rueda, P. Herrero, A.R. Landa-Cánovas, J.R. Ramos-Barrado, High quality ZnO and Ga:ZnO thin films grown onto crystalline Si (1 0 0) by RF magnetron sputtering, Solar Ener. Mat. & Solar Cells 95 (2011) 2327–2334.

[11] M. Gabás, A. Landa-Cánovas, J.L. Costa-Krämer, F. Agulló-Rueda, A.R. González-Elipe, P. Díaz-Carrasco, J. Hernández-Moro, I. Lorite, P. Herrero, P. Castillero, A. Barranco, J.R. Ramos-Barrado, Differences in n-type doping efficiency between Al- and Ga-ZnO films, J. Appl. Phys. 113 (2013) 163709.

[12] P. Nunes, E. Fortunato, P. Tonello, F. Braz Fernandes, P. Vilarinho, R. Martins, Effect of different dopant elements on the properties of ZnO thin films, Vacuum 64 (2002) 281-285.

[13] B.K. Sharma, N. Khare, Stress-dependent band gap shift and quenching of defects in Al-doped ZnO films, J. Phys. D: Appl. Phys. 43 (2010) 465402.

[14] R.D. Shannon, Revised effective ionic radii and systematic studies of interatomic distances in halides and chalcogenides, Acta Cryst. A32 (1976) 751-767.

[15] H. Iwanaga, A. Kunishige, S. Takeuchi, Anisotropic thermal expansion in wurtzite type crystals, J. Mater. Sci. 35 (2000) 2451-2454.

[16] H. Watanabe, N. Yamada, M. Okaji, Linear Thermal Expansion Coefficient of Silicon from 293 to 1000 K, Int. J. Thermophysics 25 (2004) 221-236.

[17] T. Damen, S. Porto, B. Tell, Raman effect in zinc oxide, Phys. Rev. 142 (1966) 570–574.

[18] R.H. Callender, S.S. Sussman, M. Selders, R.K. Chang, Dispersion of Raman cross section in CdS and ZnO over a wide energy range, Phys. Rev. B 7 (1973) 3788-3798.

[19] M. Tzolov, N. Tzenov, D. Dimova-Malinovska, M. Kalitzova, C. Pizzuto, G. Vitali, G. Zollo, I. Ivanov, Vibrational properties and structure of undoped and Al-doped ZnO films deposited by RF magnetron sputtering, Thin Solid Films 379 (2000) 28–36.

[20] F.J. Manjón, B. Marí, J. Serrano, A.H. Romero, Silent Raman modes in zinc oxide and related nitrides,J. Appl. Phys. 97 (2005) 053516.

[21] D. Song, Effects of rf power on surface-morphological, structural and electrical properties of aluminium-doped zinc oxide films by magnetron sputtering, Appl. Surf. Sci. 254 (2008) 4171–4178.

[22] F.J. Manjón, K. Syassen, R. Lauck, Effect of pressure on phonon modes in wurtzite zinc oxide, High Press. Res. 22 (2002) 299-304.

[23] D. Köhl, M. Luysberg, M. Wuttig, Highly textured zinc oxide films by room temperature ion beam assisted deposition, Phys. Status Solidi RRL 3, (2009) 236-238.

Figure 1

Click here to download high resolution image

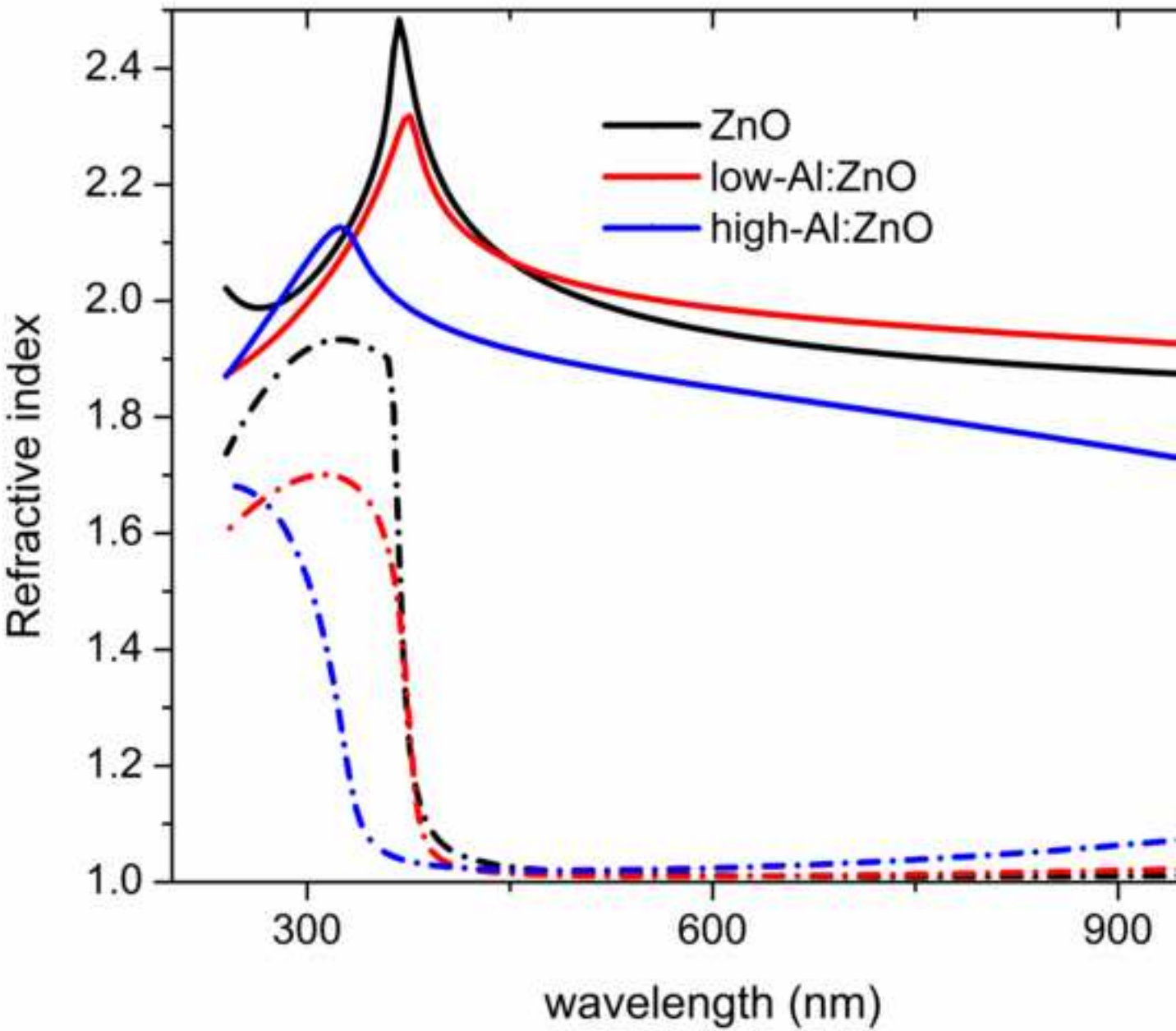

Figure 2 left

Click here to download high resolution image

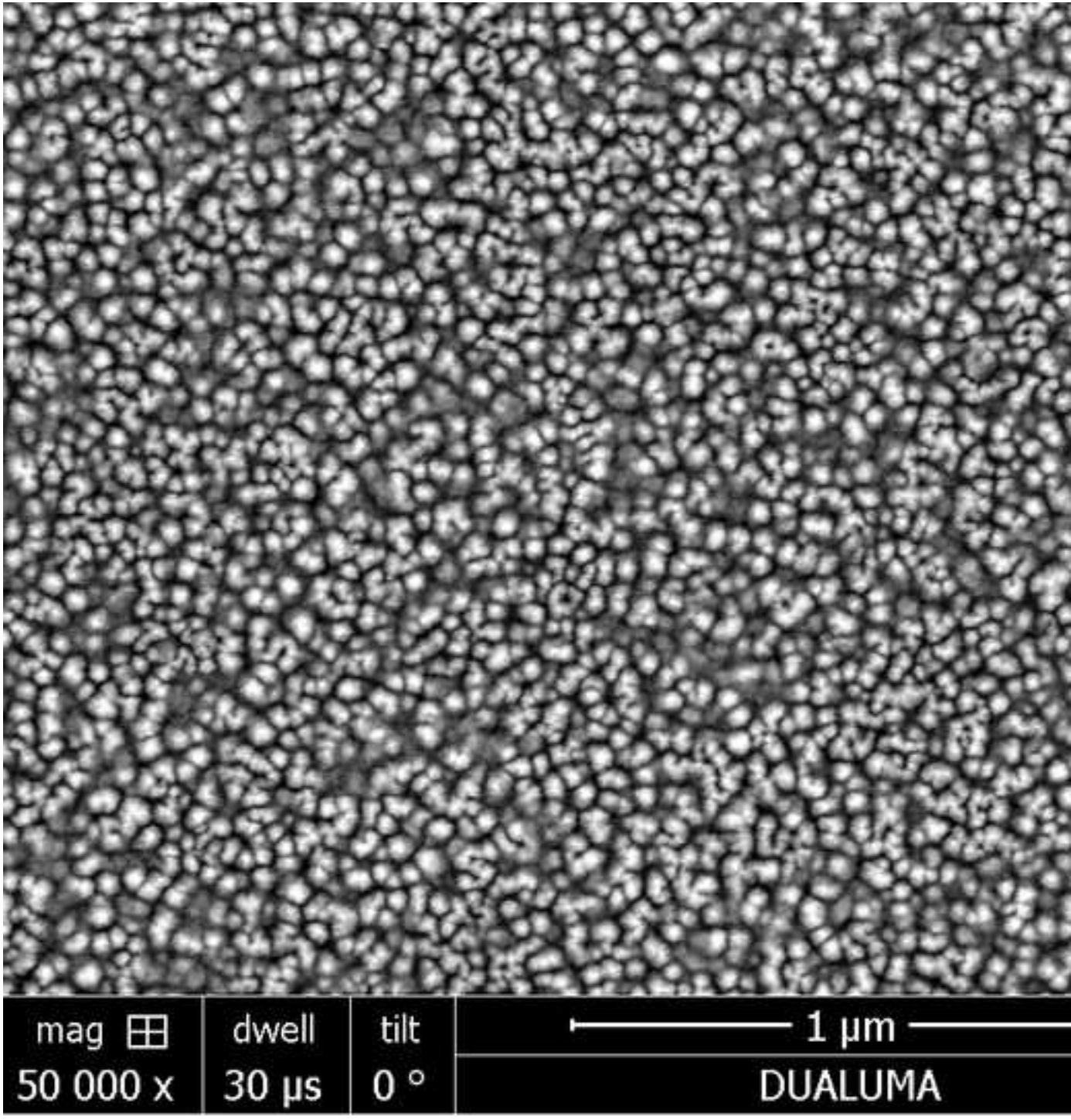

Figure 2 right

Click here to download high resolution image

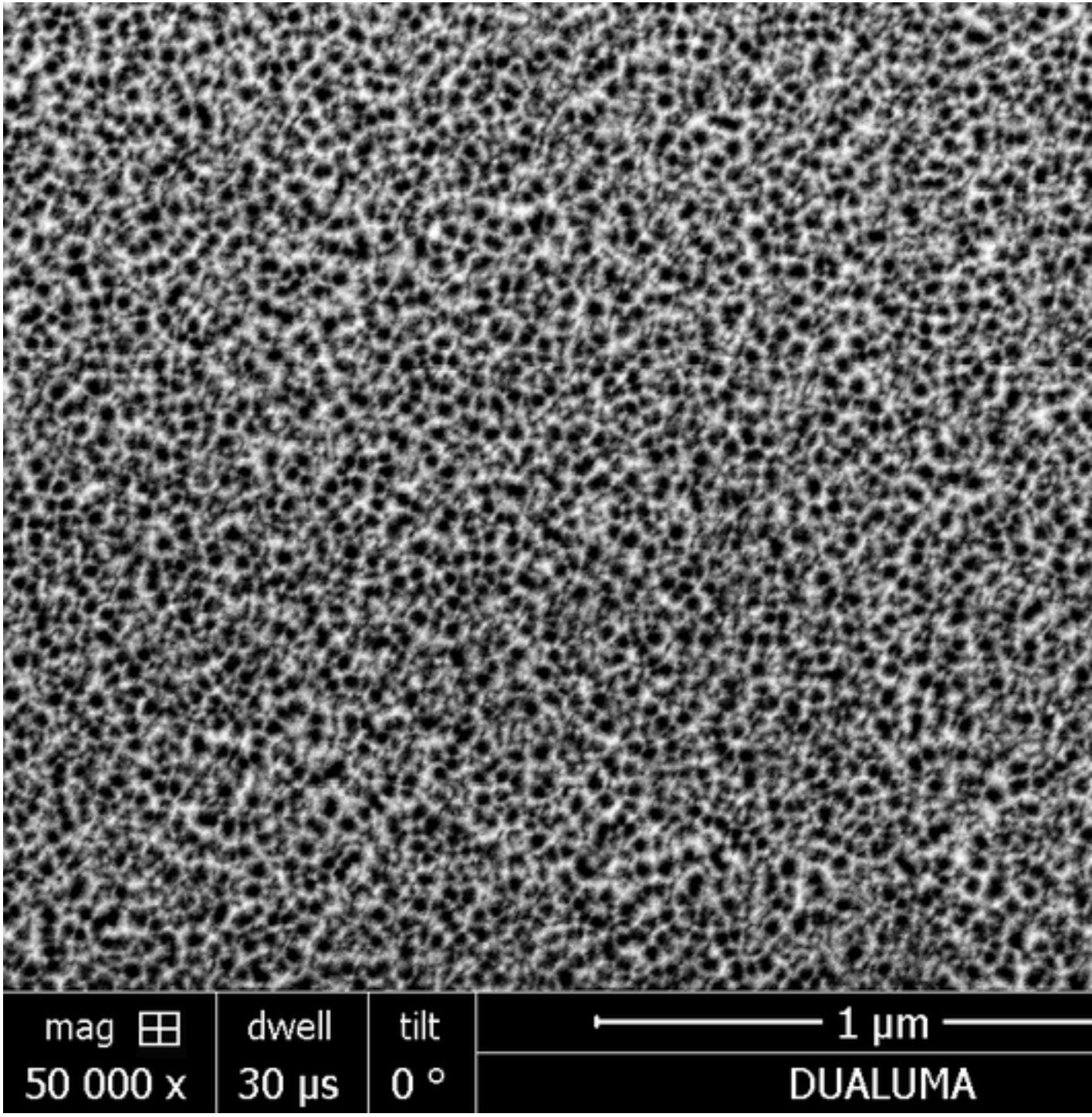

Figure 3

Click here to download high resolution image

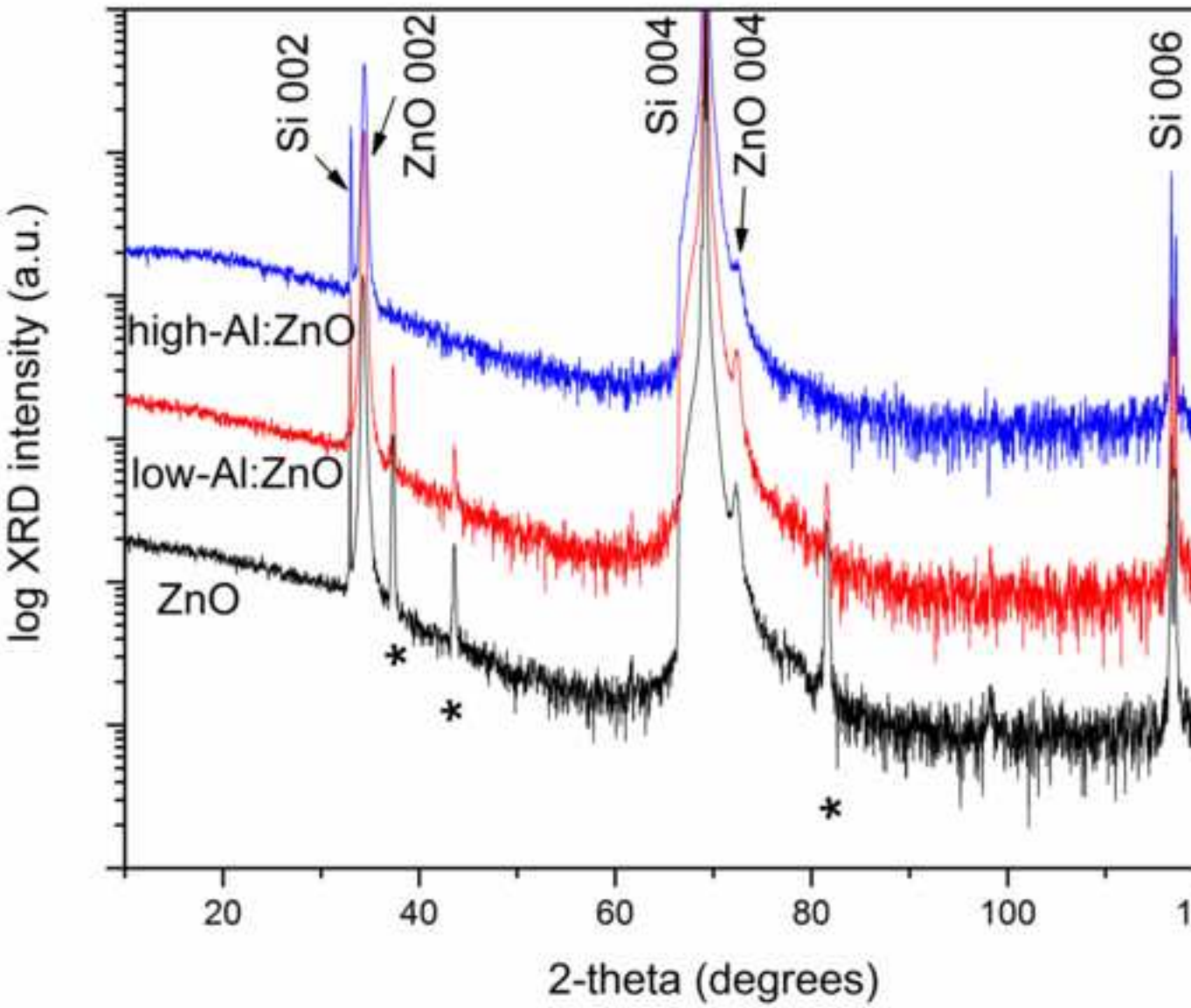

Figure 4

Click here to download high resolution image

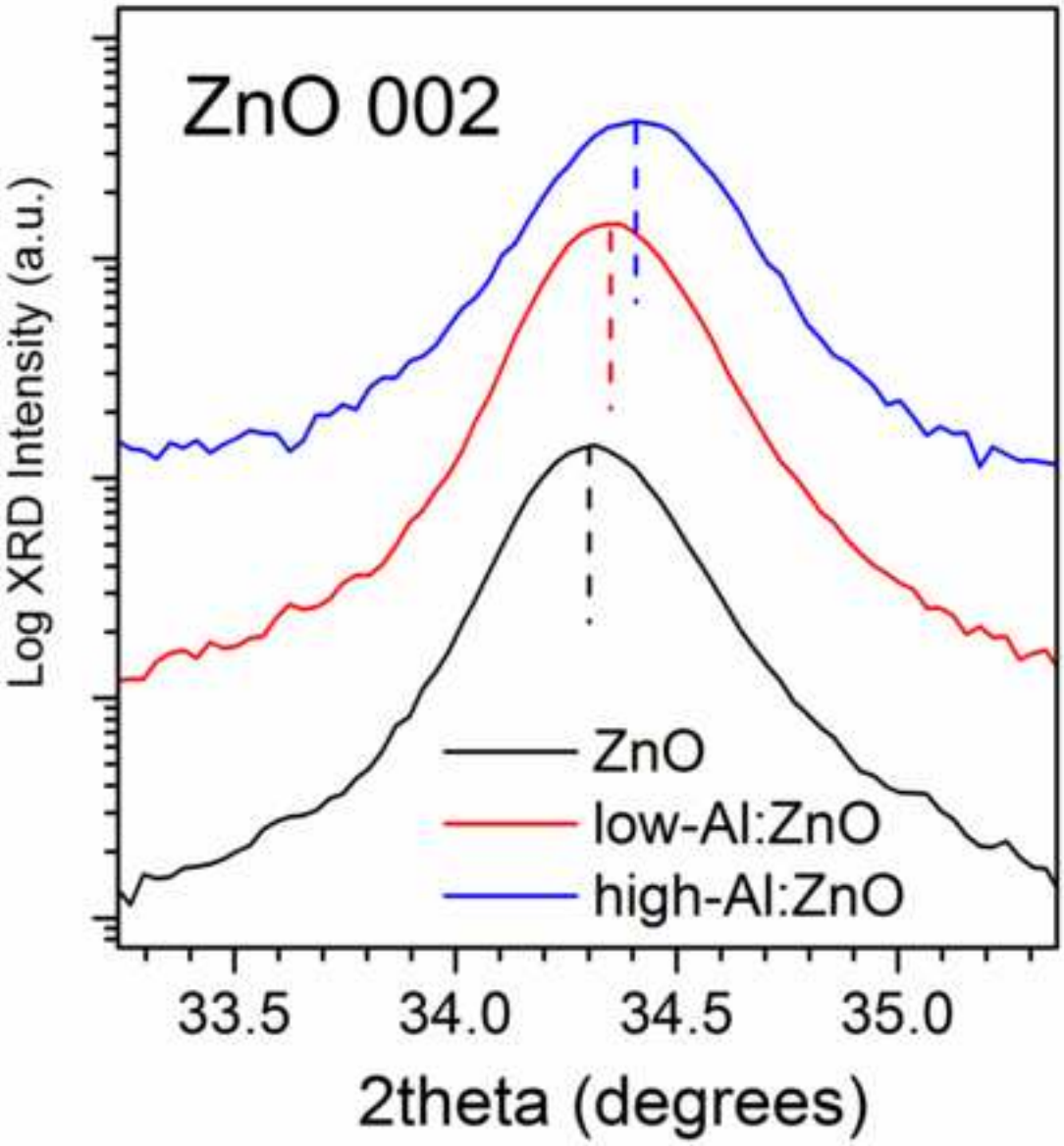

Figure 5 left

Click here to download high resolution image

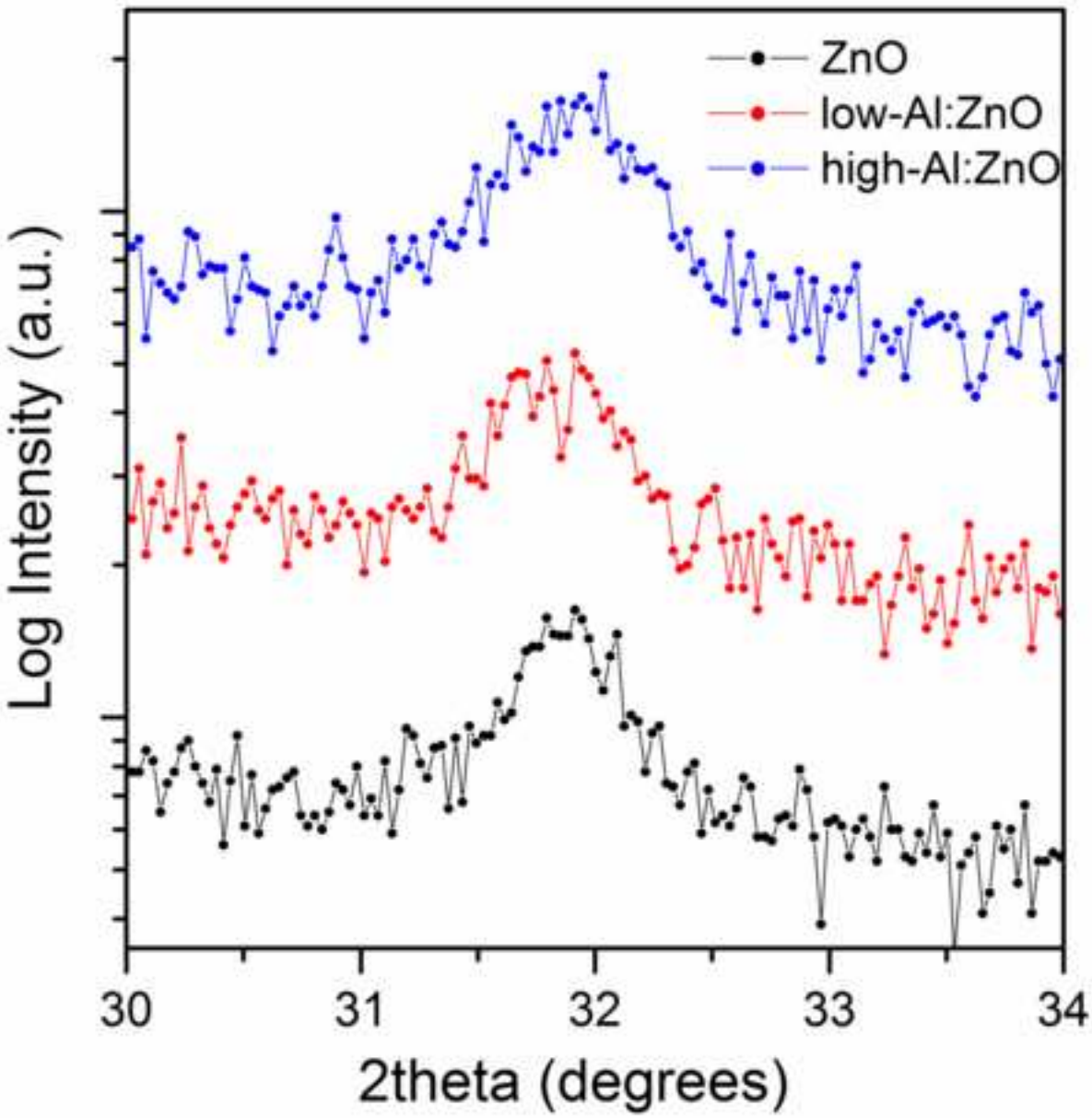

Figure 5 right

Click here to download high resolution image

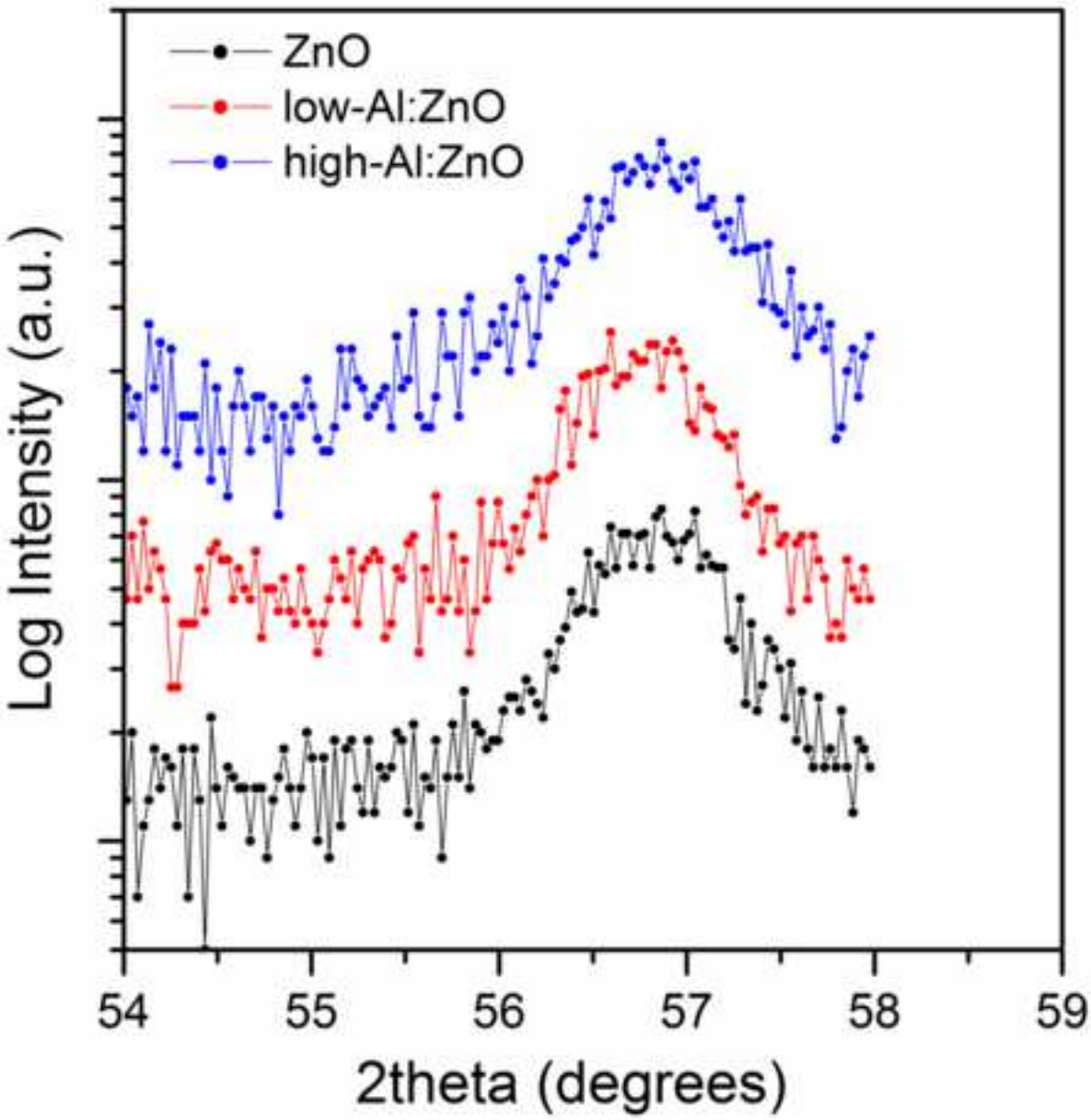

Figure 6

Click here to download high resolution image

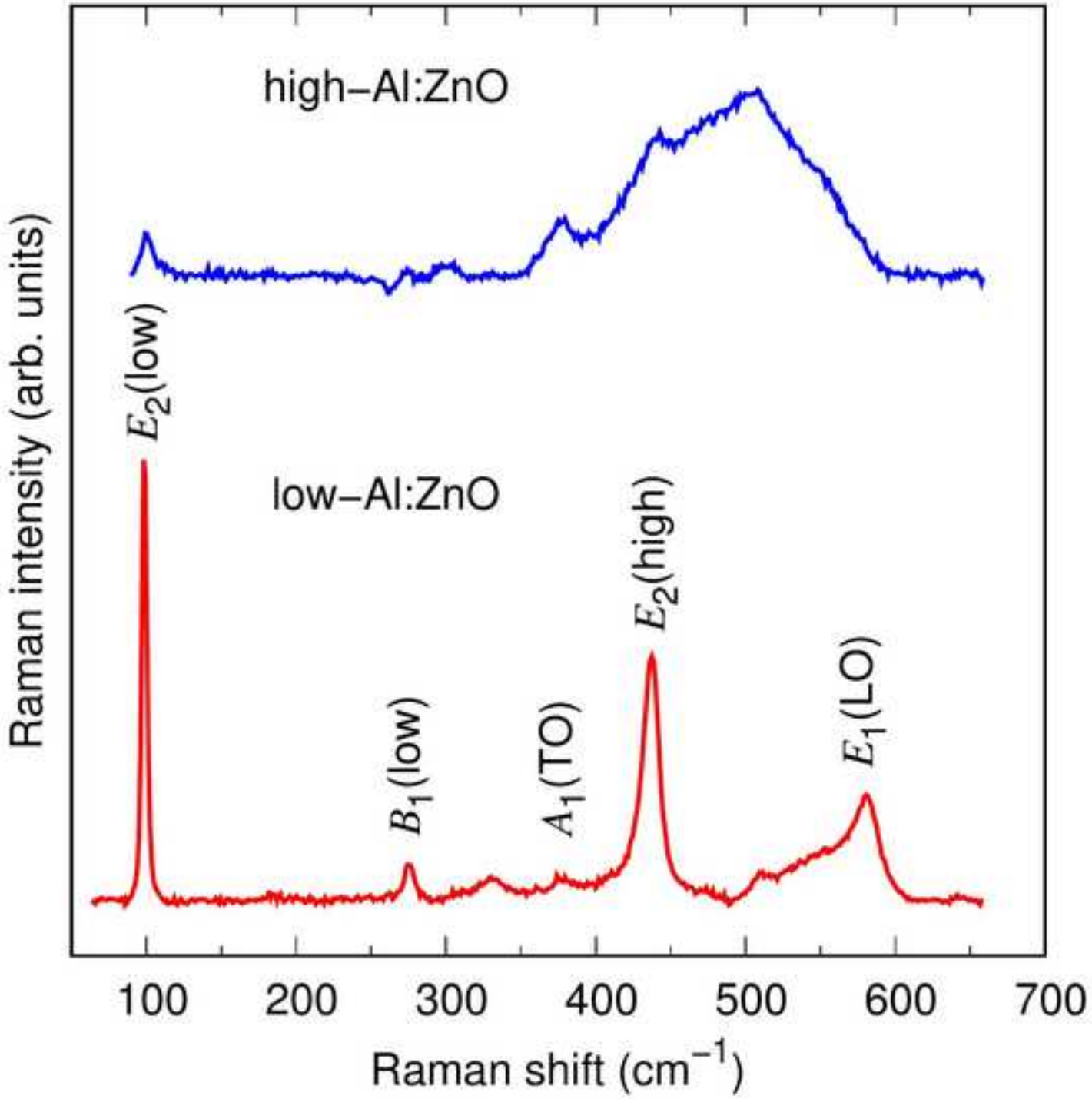

Figure 7 top left
Click here to download high resolution image

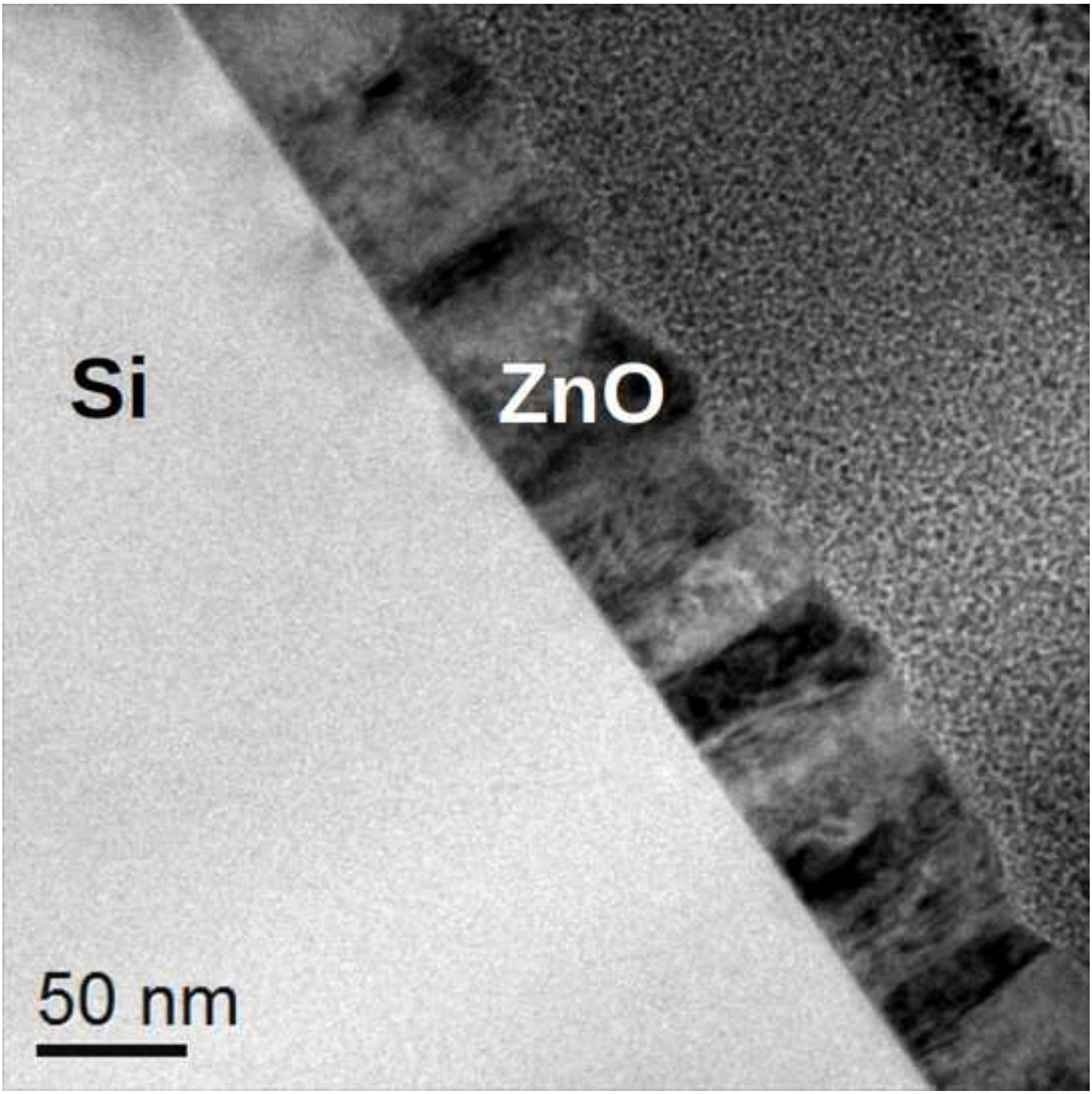

Figure 7 top right

Click here to download high resolution image

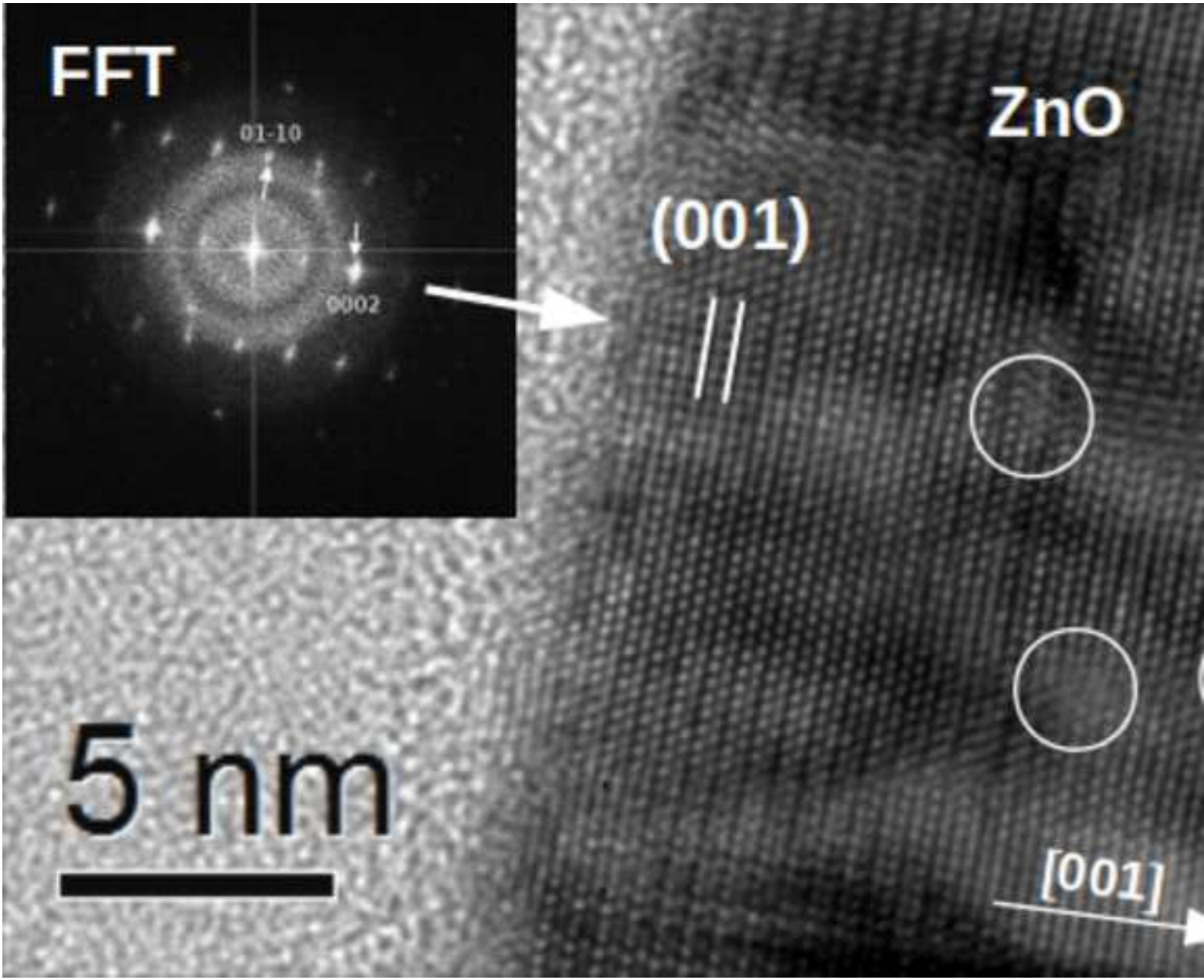

Figure 7 bottom left

Click here to download high resolution image

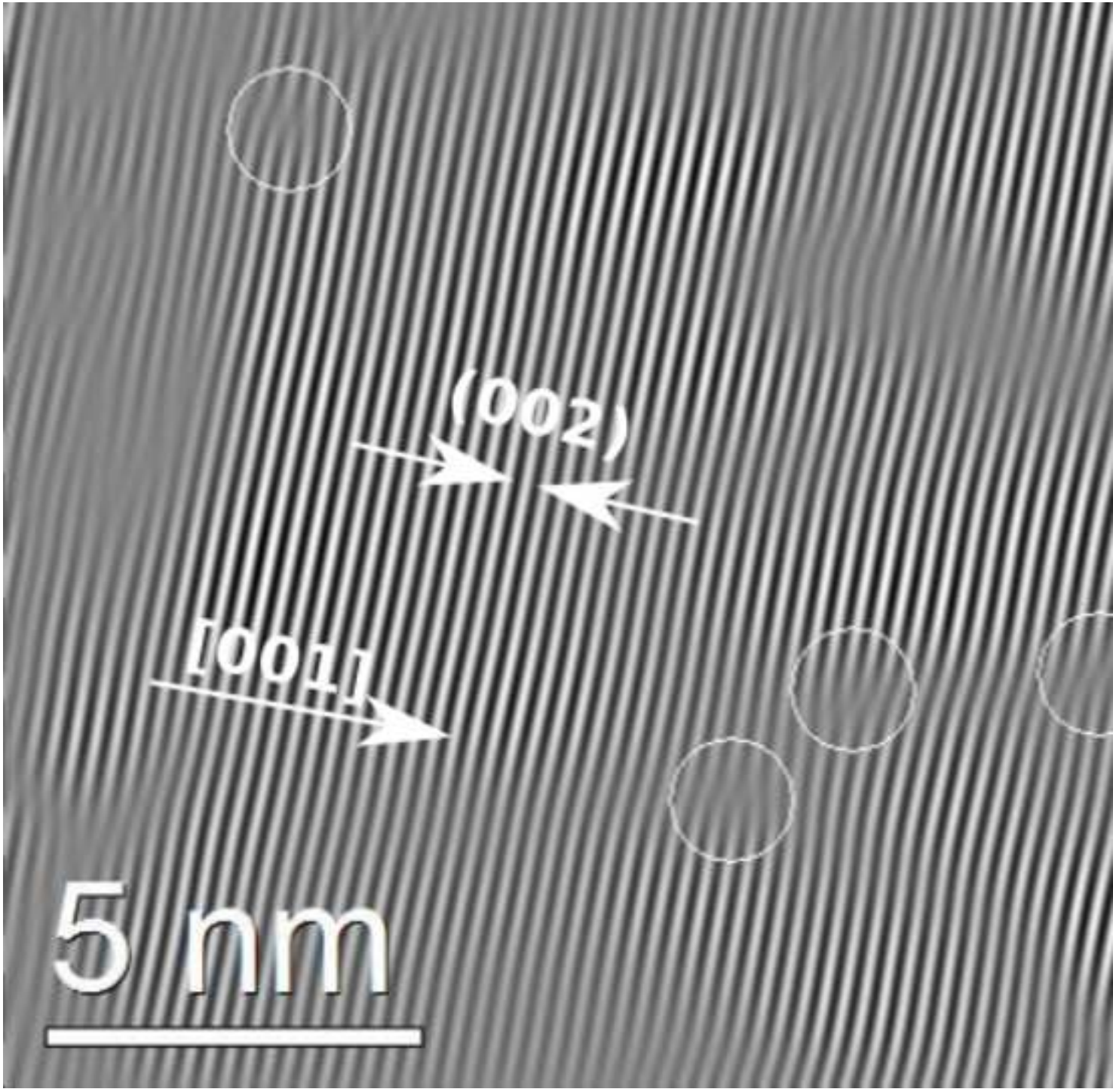

Figure 7 bottom right

Click here to download high resolution image

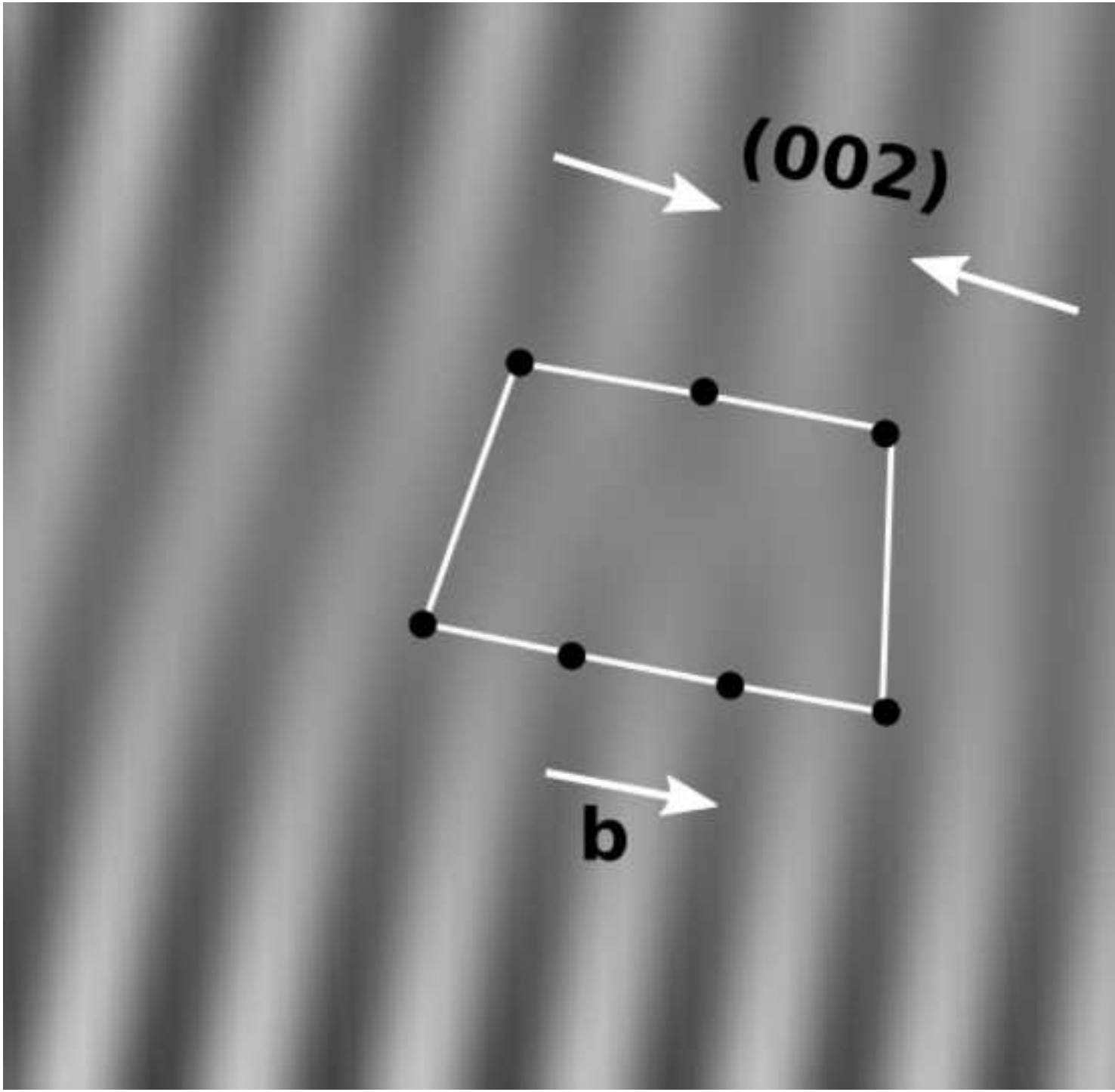

Figure 8 top

Click here to download high resolution image

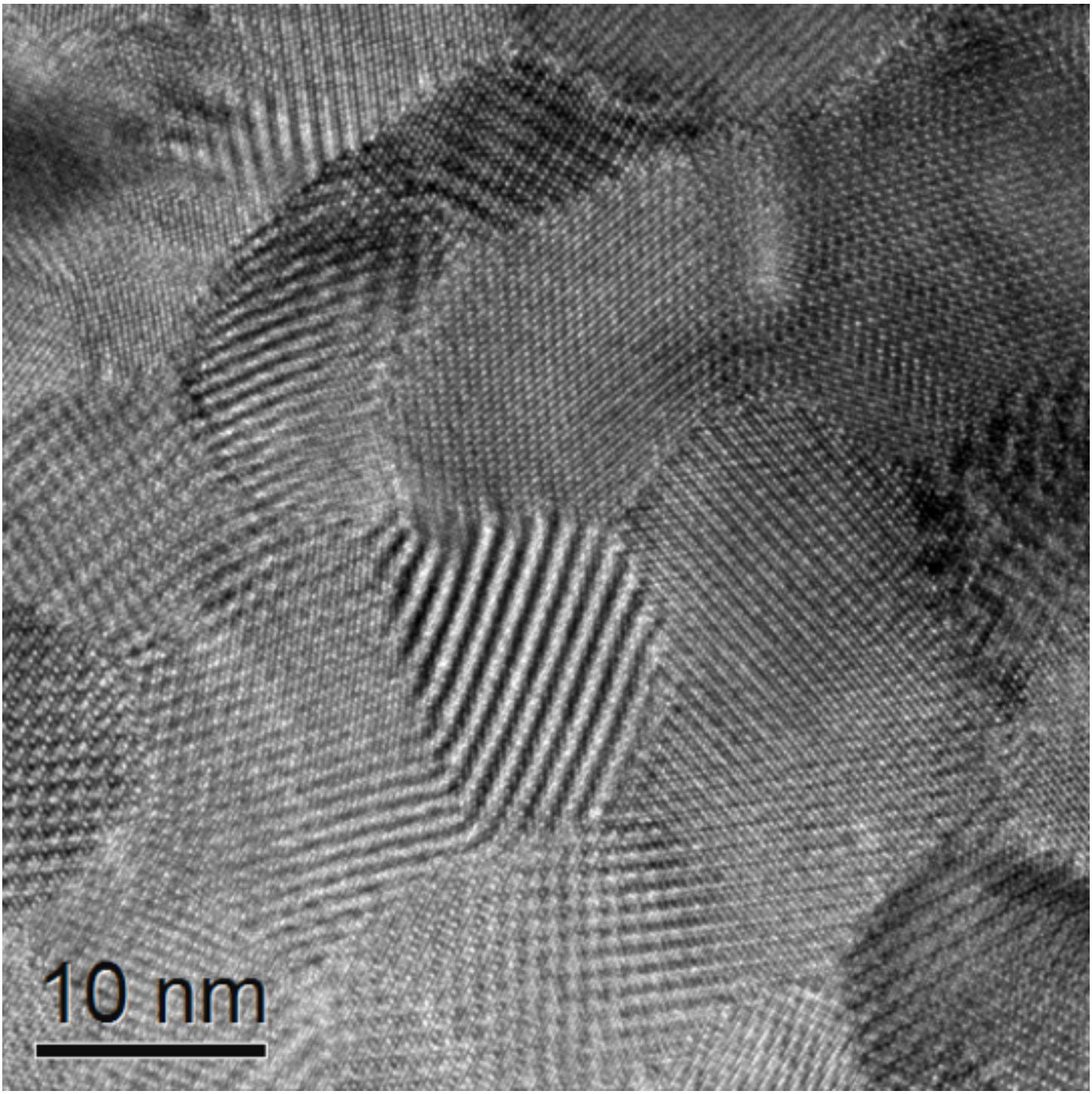

Figure 8 middle

Click here to download high resolution image

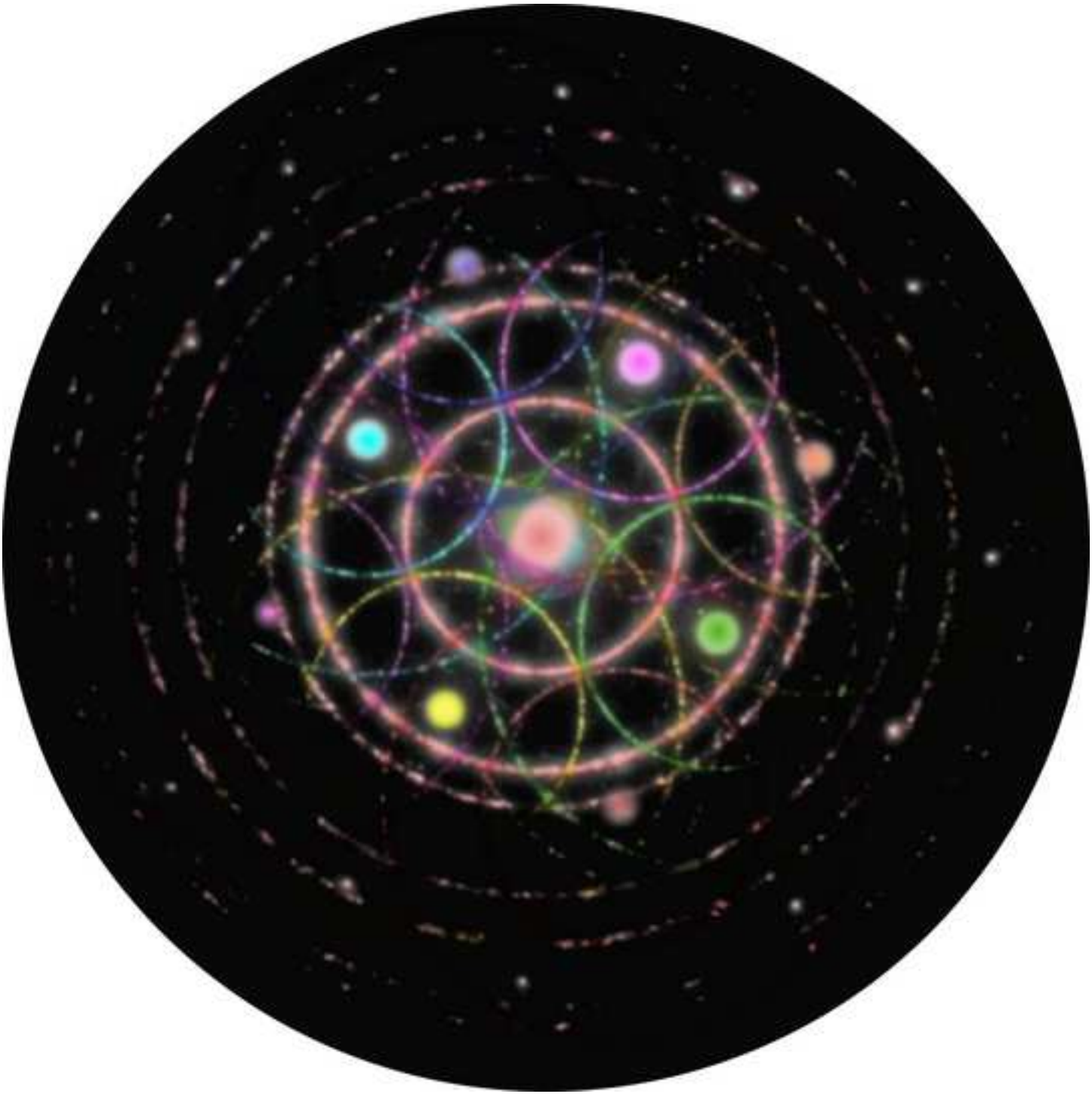

Figure 8 bottom

Click here to download high resolution image

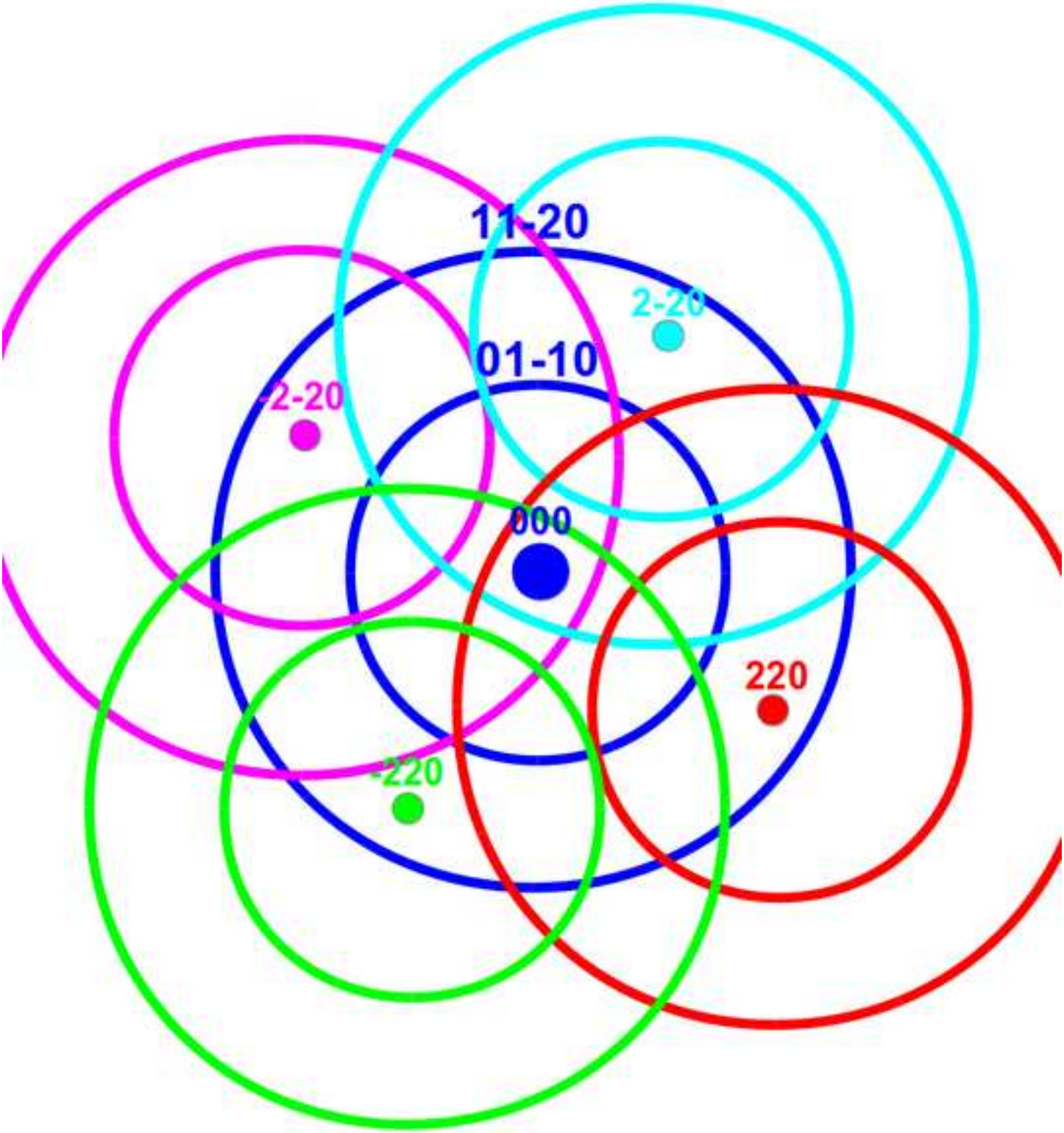

Figure 9

Click here to download high resolution image

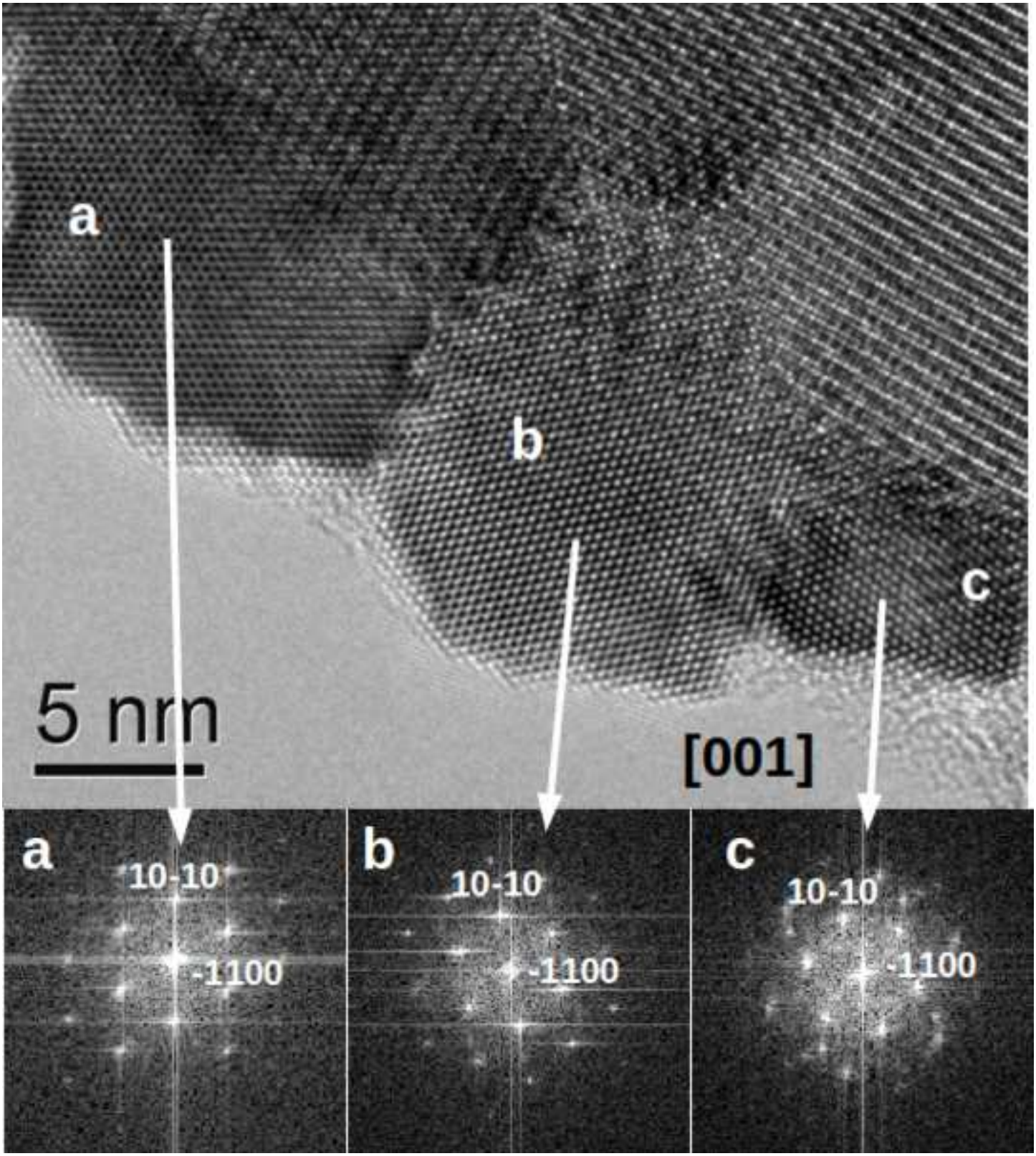

Figure 10 top

Click here to download high resolution image

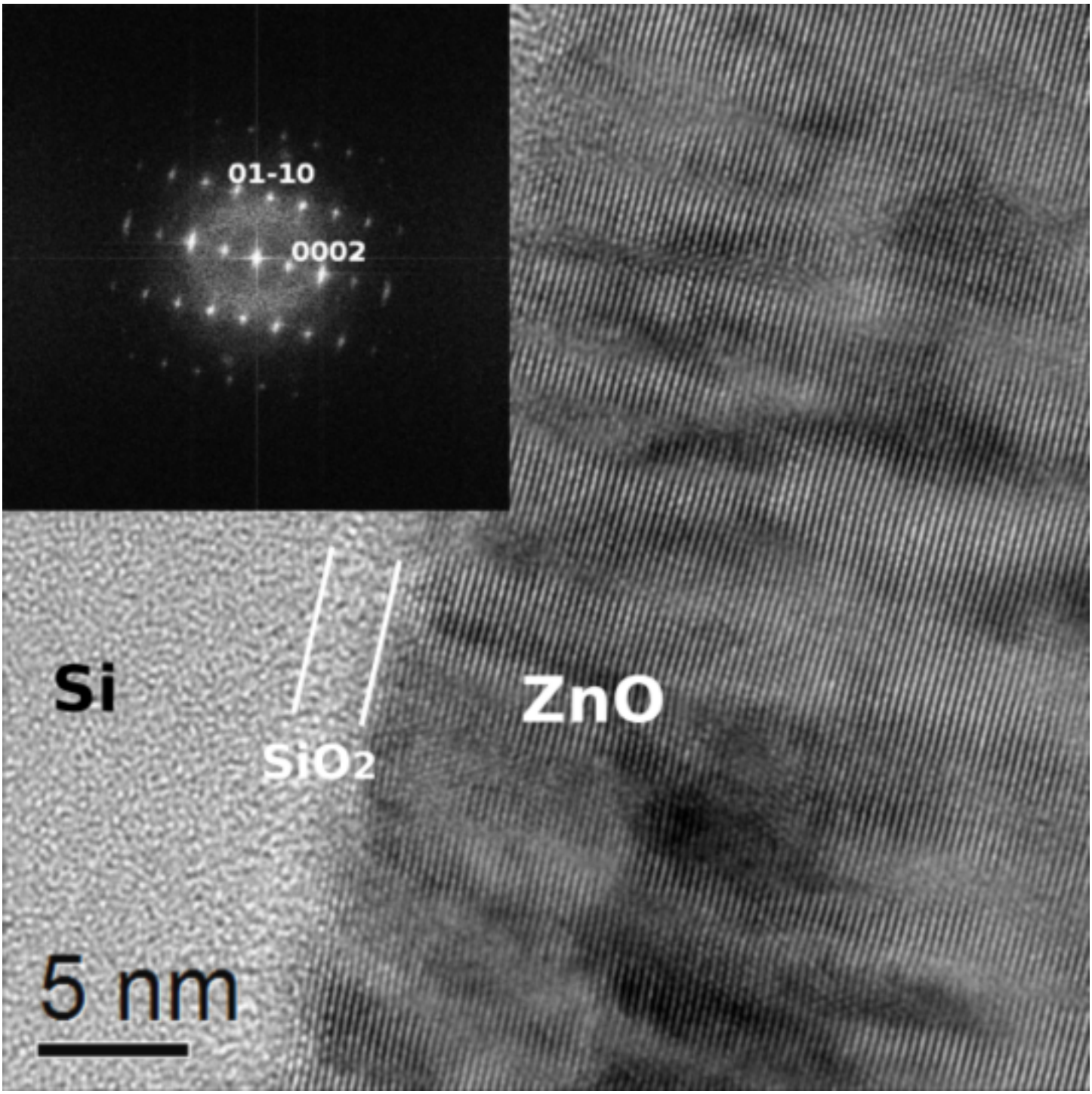

Figure 10 bottom

Click here to download high resolution image

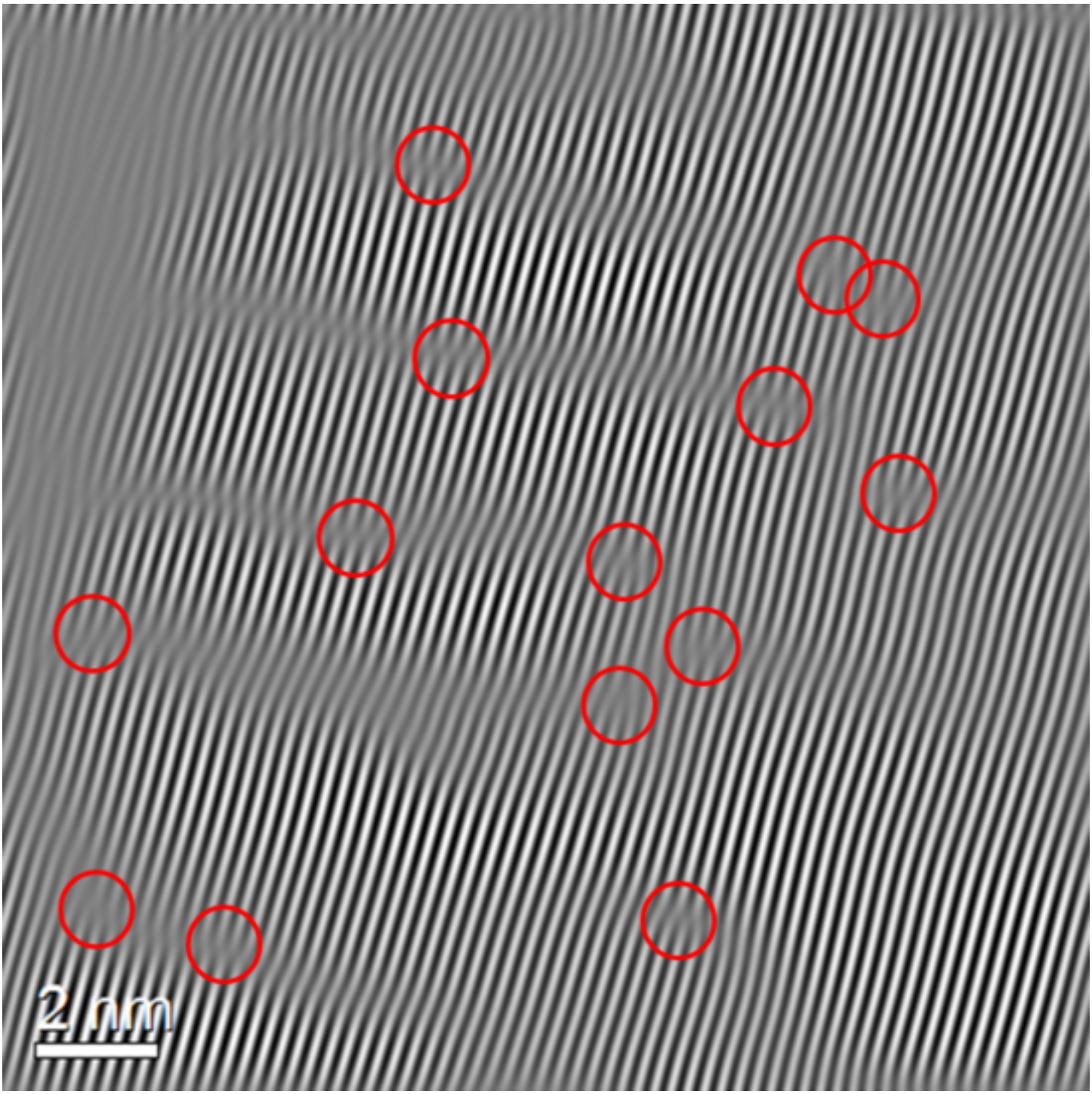

Figure 11 top

Click here to download high resolution image

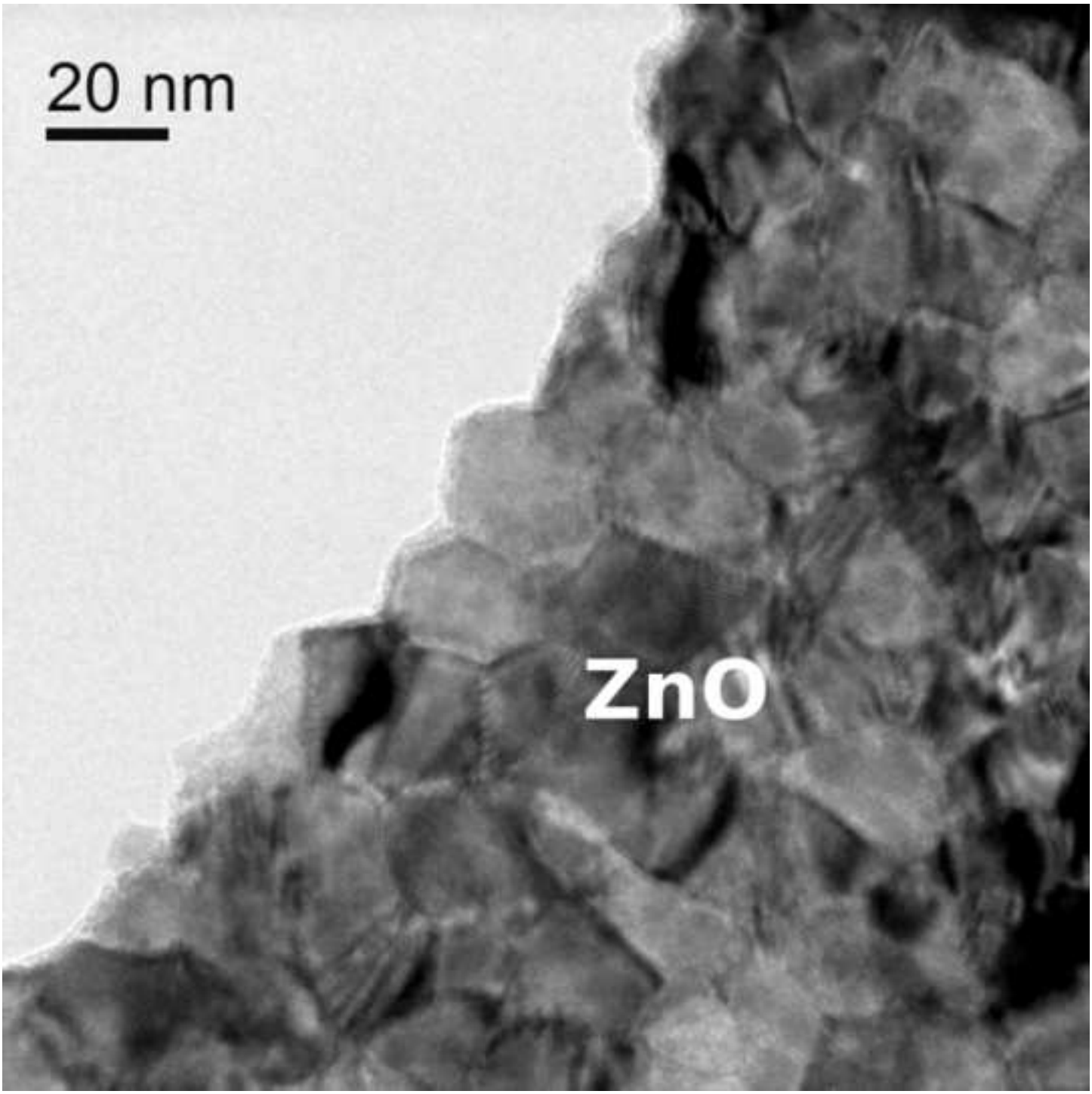

Figure 11 bottom

Click here to download high resolution image